In silico identification and experimental validation of novel anti-Alzheimer's multitargeted ligands from marine source featuring a "2-amino-imidazole plus aromatic group" scaffold

Journal:	*ACS Chemical Neuroscience*
Manuscript ID	cn-2017-004169.R2
Manuscript Type:	Article
Date Submitted by the Author:	22-Feb-2018

Complete List of Authors:	Vitale, Rosa Maria; National Research Council of Italy (CNR), Institute of Biomolecular Chemistry (ICB) Rispoli, Vincenzo; University Magna Græcia of Catanzaro, Department of Health Sciences Desiderio, Doriana; University of Naples "Parthenope", Department of Movement Sciences and Wellness Sgammato, Roberta; University of Naples "Parthenope", Department of Movement Sciences and Wellness Thellung, Stefano; University of Genova, Section of Pharmacology, Department of Internal Medicine and Center of Excellence for Biomedical research (CEBR) Canale, Claudio; University of Genova, Department of Physics Vassalli, Massimo; National Research Council, Institute of Biophysics Carbone, Marianna; National Research Council of Italy (CNR), Institute of Biomolecular Chemistry (ICB) Ciavatta, Maria Letizia; National Research Council of Italy (CNR), Institute of Biomolecular Chemistry (ICB) Mollo, Ernesto; National Research Council of Italy (CNR), Institute of Biomolecular Chemistry (ICB) Felicità, Vera; National Research Council of Italy (CNR), Institute of Biomolecular Chemistry (ICB); University Magna Græcia of Catanzaro, Dipartimento di "Scienza della Salute" Arcone, Rosaria; University of Naples "Parthenope", Department of Movement Sciences and Wellness; CEINGE - Advanced Biotechnologies s.c.a r.l. Gavagnin, Margherita; National Research Council of Italy (CNR), Institute of Biomolecular Chemistry (ICB) Masullo, Mariorosario; University of Naples "Parthenope", Department of Movement Sciences and Wellness; CEINGE - Advanced Biotechnologies s.c.a r.l. Florio, Tullio; University of Genova, Section of Pharmacology, Department of Internal Medicine and Center of Excellence for Biomedical research (CEBR) Amodeo, Pietro; National Research Council of Italy (CNR), Institute of Biomolecular Chemistry (ICB)

In silico identification and experimental validation of novel anti-Alzheimer's multitargeted ligands from marine source featuring a "2-amino-imidazole plus aromatic group" scaffold

Rosa Maria Vitale[§a], Vincenzo Rispoli[§b], Doriana Desiderio[c], Roberta Sgammato[c], Stefano Thellung[d], Claudio Canale[e], Massimo Vassalli[f], Marianna Carbone[a], Maria Letizia Ciavatta[a], Ernesto Mollo[a], Vera Felicità[a,b], Rosaria Arcone[c,g], Margherita Gavagnin Capoggiani[a], Mariorosario Masullo[c,g], Tullio Florio[d], Pietro Amodeo[a*]

[a] *Institute of Biomolecular Chemistry (ICB), National Research Council (CNR), Comprensorio Olivetti, Ed.70, Via Campi Flegrei, 34 - I-80078 Pozzuoli (NA), Italy*
[b] *Department of Health Sciences, University Magna Grœcia of Catanzaro, Building of Biosciences, University Campus "Salvatore Venuta", Viale Europa, I-88100 Catanzaro (CZ), Italy*
[c] *Department of Movement Sciences and Wellness University of Naples "Parthenope", Via Medina 40, I-80133 Naples (NA), Italy.*
[d] *Section of Pharmacology, Department of Internal Medicine and Center of Excellence for Biomedical research (CEBR), University of Genova, Viale Benedetto XV 2, I-16132 Genoa (GE), Italy*
[e] *Department of Physics, University of Genova, Via Dodecaneso 33, I-16146, Genoa (GE), Italy*
[f] *Institute of Biophysics, National Research Council, Via De Marini, 10, I-16149 Genoa (GE), Italy*
[g] *CEINGE - Advanced Biotechnologies s.c.a r.l., Via Gaetano Salvatore,486 - I-80145 Naples (NA), Italy*
[§] *These authors contributed equally.*

ABSTRACT

Multitargeting/polypharmacological approaches, looking for single chemical entities retaining the ability to bind two or more molecular targets, are a potentially powerful strategy to fight complex, multifactorial pathologies. Unfortunately, the search for multiligand agents is challenging, because only a small subset of molecules contained in molecular databases are bioactive, and even fewer are active on a preselected set of multiple targets. However, collections of natural compounds feature a significantly higher fraction of bioactive molecules than synthetic ones. In this view, we searched our library of 1,175 natural compounds from marine sources for molecules including a 2-aminoimidazole+aromatic group motif, found in known compounds active on single relevant targets for Alzheimer's disease (AD). This identified two molecules, a pseudozoanthoxanthin (**1**) and a bromo-pyrrole alkaloid (**2**), which were predicted by a computational approach to possess interesting multitarget profiles on AD target proteins. Biochemical assays experimentally confirmed their biological activities. The two compounds inhibit acetylcholinesterase, butyrylcholinesterase and β-secretase enzymes in high- to sub-micromolar range. They are also able to prevent and revert β-Amyloid (Aβ) aggregation of both $A\beta_{1-40}$ and $A\beta_{1-42}$ peptides, with **1** being more active than **2**. Preliminary *in vivo* studies suggest that compound **1** is able to restore cholinergic cortico-hippocampal functional connectivity.

Keywords: Drug Discovery, Molecular Modelling, Alzheimer's Disease, Natural Product, Multi-ligand

INTRODUCTION

Alzheimer's disease (AD), the most common cause of dementia in the elderly population, is a complex neurodegenerative disorder of the central nervous system, characterized by progressive and irreversible degeneration of cholinergic neurons, leading to a concomitant decrease of the hippocampal and cortical acetylcholine (ACh) levels, and by the presence of amyloid plaques and neurofibrillary tangles. The current pharmacological therapy for AD is mainly based on acetylcholinesterase (AChE) inhibitors (AChEI), aimed at restoring the ACh tone in the brain[1–3]. However, due to the multifactorial aetiology of this pathology, compounds able to act simultaneously on two or more relevant biological targets are highly desirable. Besides AChEI, also butyrylcholinesterase (BuChE) inhibitors (BuChEI) have been recently considered with increasing interest for the treatment of AD, since, even if BuChE role is secondary in physiological ACh metabolism, BuChE activity significantly increases with the progress of the disease[4]. Clinical trials have demonstrated a reduced cortical atrophy and attenuated loss of brain volumes in patients treated with rivastigmine, an inhibitor of both ChE enzymes[5]. A complementary therapeutic approach for AD is based on the prevention of the progressive aggregation and deposition of Aβ by decreasing its synthesis through inhibition of β-secretase (BACE-1)[6], an aspartyl protease involved in the first and rate-limiting step of Aβ formation from its amyloid precursor protein, and/or hampering Aβ aggregation, a pharmacological approach recently receiving great attention by researchers in this field[7–9].

The present work originates from the previous identification of a pseudozoanthoxanthin analog from the zoanthid crust coral *Parazoanthus axinellae*, as an AChEI[10] and from the observation that the 2-amino-imidazole group occurring in this compound is also found in known BACE-1 inhibitors[11]. These findings prompted us to search molecules sharing a similar scaffold in ICB-CNR (Pozzuoli, Italy) collection of natural marine compounds and, in view of the potential interest of multitargeting in AD therapy, to explore the potentiality of the newly-selected molecules as multiligand agents, widening the range of potential targets to BuChE and BACE-1[12–14], and investigating their ability of inhibiting Aβ aggregation. Furthermore, in case of success, the choice of a simple scaffold featuring the 2-amino-imidazole group would exhibit considerable advantages for further developments, since it both occurs in several classes of natural compounds[15], and represents a versatile and well-known synthetic scaffold[16].

In particular, here we describe: (a) the identification of putative AChE/BuChE/BACE-1

multiligands by an *in silico* approach, (b) a computational prediction of their possible binding modes and corresponding structure-activity relationships with AChE, BuChE, BACE-1, (c) their *in vitro* experimental validation by inhibition assays on both the aforementioned enzymes, and the β-amyloid aggregation and (d), in the case of compound **1**, a preliminary *in vivo* study. The overall results point to these molecules as lead compounds with interesting multitarget profiles potentially useful in the treatment of AD.

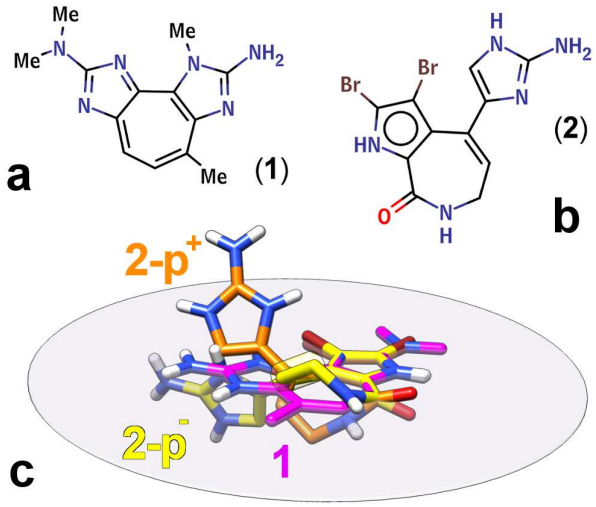

Figure 1. Structures of compounds 1 (a) and 2 (b) and rotamers of compound 2 (c). *A superposition of the 3D structure of **1** (C atoms in magenta) and the two rotamers of the seven-membered ring of **2**: 2-p$^+$ (C in orange) and 2-p$^-$ (C in yellow). The ring bond defining the sign of the two rotamers is enclosed in a transparent cylinder in 2-p$^-$. A transparent disc emphasizes the planarity of **1** and the specular out-of-plane tilt of 2-p$^+$ vs. 2-p$^-$. N, O and Br atoms are painted blue, red and red-brown, respectively. H is painted white in panel **c** and according to the bonded heavy atom in panels **a-b**.*

RESULTS AND DISCUSSION

The pseudozoanthoxanthin analog from *Parazoanthus axinellae* template was ideally subdivided into a two-ring aromatic system joined to a (possibly substituted) 2-amino-imidazole group. To broaden the searched chemical space, either one- or two-ring aromatic systems and a moderate (up to two torsional angles) conformational freedom were allowed. Thus, the full version (i.e. including molecules not yet publicly accessible) of the ICB database featuring 1,175 molecules was searched for molecules simultaneously containing a 2-amino-imidazole moiety and a one- or two-ring aromatic system, filtering off those hits exhibiting more than two torsional degrees of freedom between the two groups. This search resulted in two hits, both available in suitable quantities for subsequent *in vitro* experimental validation within our natural product collection: the 2-amino-3,9-dimethyl-5-methylamino-3H-1,3,4,6-tetrazacyclopent[e]azulene (**1**), a pseudozoanthoxanthin from an unidentified caribeean zoanthid, differing from the analog reported by Turk et al.[10] in the number and

position of methyl substituents on the azulene ring (**Figure 1**), and the bromo-pyrrole alkaloid stevensine (**2**)[17] (**Figure 1**), both endowed with a cyclic scaffold and with a 2-amino-imidazole group.

Computational validation by molecular docking and dynamics of compounds 1 and 2 as possible inhibitors of AChE, BuChE and BACE-1

A combined approach of molecular docking and molecular dynamics (MD) simulations was undertaken to investigate the capabilities of compounds **1** and **2** to bind the active sites of the hAChE, hBuChE and hBACE-1. The best-ranking ligand poses (i.e. the ones with most favourable Autodock binding energy) for each of the most populated clusters in each docking run were selected for the subsequent MD simulations to assess the overall stability of the corresponding binding modes. The results obtained on each selected target are discussed in detail in the following sections.

Since **2** can adopt two different puckerings of its seven-membered cycle, featuring either positive (p^+) or negative (p^-) value of C6-C7-C8-N9 dihedral angle (**Figure 1**), and the docking programs used in this work do not implement effective procedures to sample the torsional space of a cycle, these two conformations were separately docked for all the targets.

Modeling suggests that compound 1 can bind to both CAS and PAS sites of hAChE

Docking calculations suggest that both catalytic anionic site (CAS) and peripheral anionic site (PAS) regions can be alternatively involved in **1** binding, resulting in a single (C1) **(Figure 2a**) and two (P1 and P2) **(Figure 2c-d**) most recurring poses for CAS and PAS, respectively. The stability of the three resulting complexes was assessed by 30 ns MD simulations for each system, the last 10 ns of each trajectory being used for structural and energetical analysis. The main polar interactions for each complex are listed in **Table S1** of **Supporting Information**. Poses C1, persistent during the whole MD simulation, and P1, after an initial rearrangement, are stabilized by interactions involving both the 1-methyl-2-amino-imidazole and the 2-N',N'-dimethylamino-imidazole rings of **1** (hereinafter abbreviated as Me-NH_2-Im and H-NMe_2-Im, respectively). Pose P2, quite stable during MD, spans the whole PAS site, but it is stabilized by interactions with hAChE involving only its Me-NH_2-Im 2-amino-imidazole. When comparing the predicted free energies reported in **Table S1**, it is important to note that their exact values are, in general, only meaningful to calculate differences between similar ligands (in terms of size, functional groups and internal degrees of freedom) in the same binding site of a single target protein. In fact, simpler approaches like that used in the present work totally neglect conformational entropy and include solvation contributions only

implicitly. Such approximations are still quantitatively acceptable when these terms (almost) cancel, as it occurs in the aforementioned cases, but not when they are expected to substantially differ between different binding sites, as in the case of CAS and PAS in hAChE, exhibiting substantial differences in terms of both solvent accessibility, and distribution or mobility of polar/apolar sidechains. However, even more sophisticated methods, while being significantly more computationally expensive, still do not provide quantitatively accurate estimates of those contributions in general cases. In this view, although the binding free energy predicted for the CAS pose C1 is lower than those of PAS poses, both PAS and CAS modes will be discussed, and a more quantitative use of calculated free energies will only be made in comparisons between different poses or ligands in a single binding site.

Modeling suggests that compound 2 can only bind to hAChE CAS site

The four most recurring binding poses for **2** (C1-C4) only involve the CAS region and include both **2**-p^- (C1-3) and **2**-p^+ (C4) puckering states of **2** seven-membered ring. These two states also correspond to two different interaction patterns of the 2-amino-imidazole ring (hereinafter abbreviated as H-NH_2-Im): in C1-C3 it points toward Asp74 and in C4 it forms a cationic-π/π stacking with Trp86. All the poses, after an initial rearrangement, resulted stable for the last 10 ns (out of 20 ns) of MD simulations, but only two poses exhibited an estimated binding free energy below -10 kcal mol^{-1}, i.e. p^+-C4 (-10.92±0.02 kcal mol^{-1}) **(Figure 2e)** and p^--C3 (-10.19±0.02 kcal mol^{-1}) **(Figure 2f)**; thus they were selected as representative for **2** binding modes to hAChE. While the main polar intermolecular interactions for each complex are reported in **Table S1**, a noteworthy feature of p^+-C4 is the presence of a resident water molecule that mediates the interaction between the **2** carbonyl group and Asp74 **(Figure 2e)**.

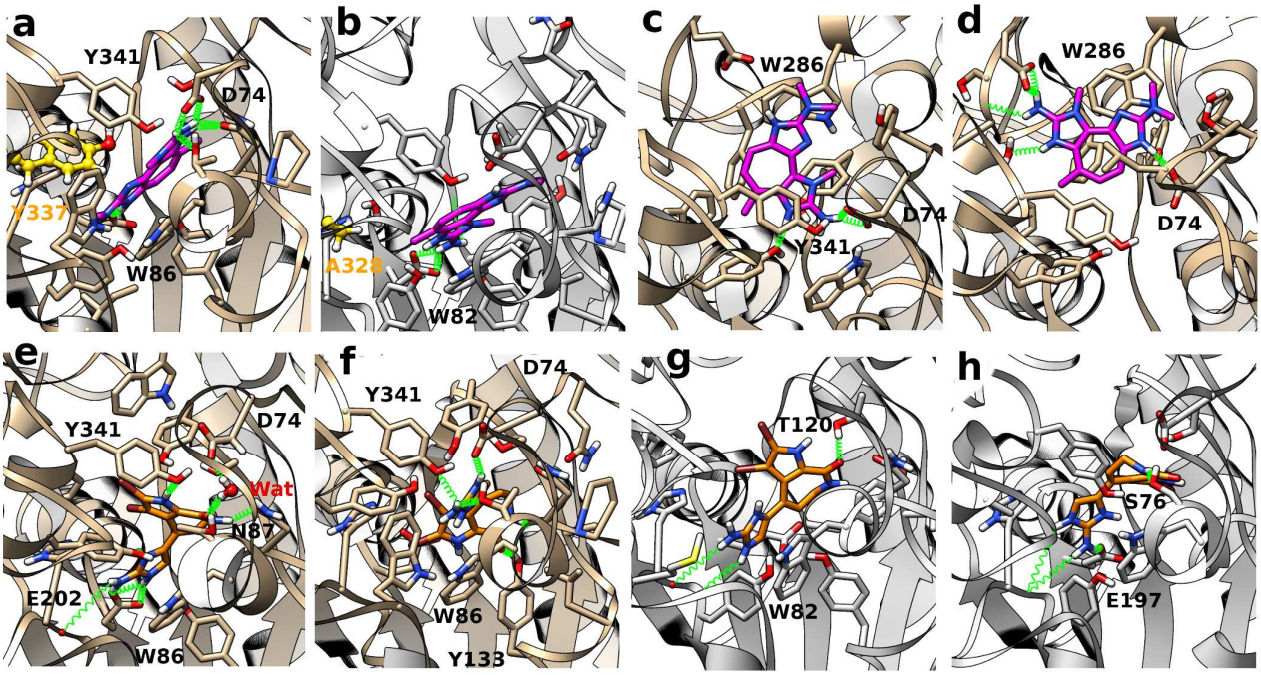

Figure 2. Representative 3D models of the hAChE/hBuChE complexes with compounds 1 and 2. *The figure shows the same view of the ligand binding site region for the main selected poses after MD refinement: C1 (**a**), P1 (**c**), P2 (**d**) for hAChE (tan C atoms) complexes with **1** (magenta C atoms), C1 for the complex between hBuChE (gray C atoms) and **1** (**b**), p^+-C4 (**e**), (**f**) p^--C3 for AChE (tan C atoms) complexes with **2** (orange C atoms) and p^+-C2 (**g**), p^--C3 (**h**) for the complex between hBuChE (gray C atoms) and **2**. Proteins are represented with ribbons plus stick sidechains for residues within 4 Å from the ligand and labels for the most relevant residues. A green spring represents stable ligand-protein H-bonds. H, N, O S and Br atoms are painted white blue, red, yellow and red-brown, respectively. Sidechains of the hAChE Tyr337 (**a**) and hBuChE Ala328 (**b**) residues, corresponding to a relevant difference between the sites of the two proteins, are shown in ball and stick representation with yellow C atoms. A bridging water molecule between **2** and Asp74 in p^+-C4 (**e**) is shown in ball and stick representation and labeled in red.*

Modeling shows a single binding mode for compound 1 to hBuChE CAS site

Docking produces a single cluster for **1** binding modes. In the representative pose (C1), quite stable during MD simulations, the ligand interacts with residues lying in the CAS region (see **Table S1** for a list of polar ligand-protein interactions), albeit with a different orientation from that adopted in the correspondent hAChE binding site, since Me-NH_2-Im ring now points toward the bottom of the catalytic pocket **(Figure 2b)**. This difference in orientation is likely due to the presence in hBuChE of Ala328 in place of Tyr337 occurring in hAChE. In fact, the smaller size of this residue, along with its hydrophobic aliphatic character, ensures a more favourable accommodation of the methyl group on the seven-membered cycle in comparison with the bulkier aromatic sidechain found in hAChE.

Modeling suggests a looser binding for compound 2 to hBuChE

From docking calculations two representative poses from the most populated clusters with better binding energy were selected for **2**-p^+ (C1,C2) and one for **3**-p^- (C3) and subjected to

MD simulations. C1 complex was quite unstable during MD, drifting away toward dissociation, while C2 and C3, after an initial rearrangement, remained stable. In p^+-C2 pose **(Figure 2g)** H-NH_2-Im engages mainly a cationic-π/π stacking with Trp82 without forming H-bond (HB) interactions with Glu197, while in p^--C3 complex **(Figure 2h)** the aforementioned aromatic interaction is less optimized, with H-NH_2-Im group engaging a HB enforced by ionic interactions with Glu197. Other polar interactions engaged by the ligand in the two complexes are reported in **Table S1**. By comparing the same ligand orientation in hAChE and hBuChE complexes, the amino acid substitution Tyr337 → Ala328 and Tyr121 → Gln119 result not only in a loss of direct polar interactions engaged by these residues with the ligand (H-bond and π stacking, respectively), but also in less optimized simultaneous interactions with both Trp and Glu residues, occurring instead in hAChE complex.

Thus, overall, modelling predicts similar binding strength for hAChE-**1**, hAChE-**2** and hBuChE-**1** complexes and a weaker binding for BuChE-**2**. The size of the CAS site, larger in hBuChE than in hAChE, that does not allow a tight binding of **2**, differently from **1**, which features a larger aromatic/cationic system, able to productively interact even with the wider hBuChE CAS.

***In vitro* hAChE and eqBuChE inhibition assays support modelling predictions, demonstrating differential activity of compounds 1 and 2 on the two targets**

The inhibitory ability of the compounds on both hAChE and eqBuChE activities were tested in the absence or in the presence of different concentrations of **1** and **2,** respectively. EqBuChE and hBuChE share more than 90% of sequence identity and, above all, the residues involved in the interaction with both compounds are fully conserved. Thus eqBuChE represents a good experimental model to validate the computational results. The results reported in **Figure S1a** (see **Supporting Information**) indicated that **1** exhibited a lower inhibitory activity than **2** on hAChE; an opposite behavior was observed for eqBuChE (**Figure S1b**), for which **1** exhibited a greater inhibitory activity than **2**. The data from semi-logarithmic plots (not shown) allowed the calculation of the IC_{50} that are reported in **Table 1**.

Table 1. *Inhibition parameters (± standard deviation) of **1** and **2** on hAChE, eqBuChE and mBACE-1 activity. The number of replicates is indicated in parentheses. The statistical significance of mean values is evaluated with a single group t-Student test: t probability value* $^{*}< 0.0001$, $^{**}< 0.01$; $^{***}< 0.05$.

	1		**2**	
Activity	**IC_{50} (μM)**	**K_i (μM)**	**IC_{50} (μM)**	**K_i (μM)**
hAChE	$12.2 \pm 1.4\ (3)^{**}$	$11.7 \pm 2.8\ (20)^{*}$	$7.8 \pm 1.5\ (3)^{***}$	$8.1 \pm 2.7\ (8)^{*}$
eqBuChE	$14.6 \pm 5.4\ (5)^{**}$	$17.5 \pm 8.1\ (19)^{*}$	$141.6 \pm 34.0\ (4)^{**}$	$96.9 \pm 56.3\ (19)^{*}$
mBACE-1	$0.9 \pm 0.1\ (3)^{**}$		$1.4 \pm 0.4\ (3)^{***}$	

In order to characterize the kinetic features of inhibition, the effects of different concentrations of the two inhibitors were tested at different thiolated substrate concentrations. The data indicate that the presence of the inhibitors do not affect the enzyme affinity for the substrate, whereas it provokes a reduction in the V_{max} value (not shown). The values of inhibition constants (K_i) calculated using different methods were mediated and shown in **Table 1** for comparative purposes. Compound **1** exhibits a lower activity on hAChE, but a stronger inhibition on eqBuChE than **2**, thus confirming the results reported in **Figure S1**.

A possible "internal decoy" effect could explain quantitative differences in inhibitory activity of 1 and 2 toward hAChE

Compound **2** exhibits an inhibitory activity toward hAChE in the same micromolar range, but greater than **1**, in spite of the most favourable binding free energy (by ~3 kcal/mol) predicted for **1** in the CAS site. However, the distribution of the two ligands in the binding site resulting from docking into hAChE shows that, while **2** only binds the CAS site, **1** can alternatively binds either CAS or PAS. Since it is well-known that PAS inhibitors are less efficient than CAS ones, the apparent drop in inhibitory activity from **1** to **2** could be explained by an "internal decoy" action of the PAS region on compound **1**. Binding to PAS, in fact, reduces the effective amount of ligand available to the more effective CAS binding, thus leading to the observed reduction of the "effective" overall experimental inhibition-related parameters.

Modeling shows possible binding of compound 1 to both "open" and "closed" states of hBACE-1 active site

Since a class of not-peptidic BACE-1 inhibitors features the 2-amino-imidazole group, a docking study was also carried out on this target for both the molecules to evaluate their potential ability as BACE-1 inhibitors. BACE-1 belongs to the aspartic protease family, characterized by a β-hairpin flap covering the active site that contributes to the hydrolytic specificity. This flap can assume two main conformations, associated to different relative orientations to the protein active site and usually named "open" or "closed" state after the higher or lower accessibility of the active site they determine, respectively. Since they are expected to affect ligand binding properties, docking was performed on two distinct template structures, each one representative of a different flap state.

A total of five poses from docking runs were selected for the subsequent MD simulations, deriving from protein conformations with both "open" (O1-2) and "closed" (C1-3) flap.

C1 and C2 poses remain stable with respect to the starting docking orientation, whereas O1 pose collapsed onto O2 and C3 drifted away toward dissociation. The main polar interactions for each complex are reported in **Table S2** in **Supporting Information**. C1 (**Figure 3a**) and C2 (**Figure 3b**) poses are flipped each other: in C1 Me-NH_2-Im interacts with Tyr71 and both catalytic aspartate residues (Asp32 and Asp228), while the methyl group on the seven-membered cycle interacts with Phe108 and Ile118; in C2 instead, H-NMe_2-Im points toward the catalytic aspartates, while the methyl group on the seven-membered cycle now interacts with Tyr71, Thr72 and Trp115. In O2 pose (**Figure 3c**), ligand Me-NH_2-Im interacts with both catalytic aspartate residues and Thr231; H-NMe_2-Im interacts with a cluster of aromatic residues (Tyr71, Phe108 and Trp115), and with Thr72.

Modeling suggests that also compound 2 can bind to both "open" and "closed" states of hBACE-1 site

From docking runs carried out on hBACE-1 protein with the flap loop in closed conformation (PDB: 2QZL), two poses were selected for **2**-p^- (C1-C2) and one pose for **2**-p^+ (C3). The main polar interactions for each complex are listed in **Table S2**. In C1 complex (**Figure 3d**) the ligand is sandwiched between the catalytic site and the flap loop with the amino-imidazole group interacting with Asp32, Asp228 and Thr231, while the bicyclic system interacts with Thr232, Tyr71, Gln73, Phe108 and Trp115. C2 (**Figure 3e**) recapitulates all H-bonds interactions engaged by 2-amino-imidazole ring of C1 but adopts a different orientation of the macrocycle which now does not interact with the flap loop and forms HB with Lys 224 and

Thr229.

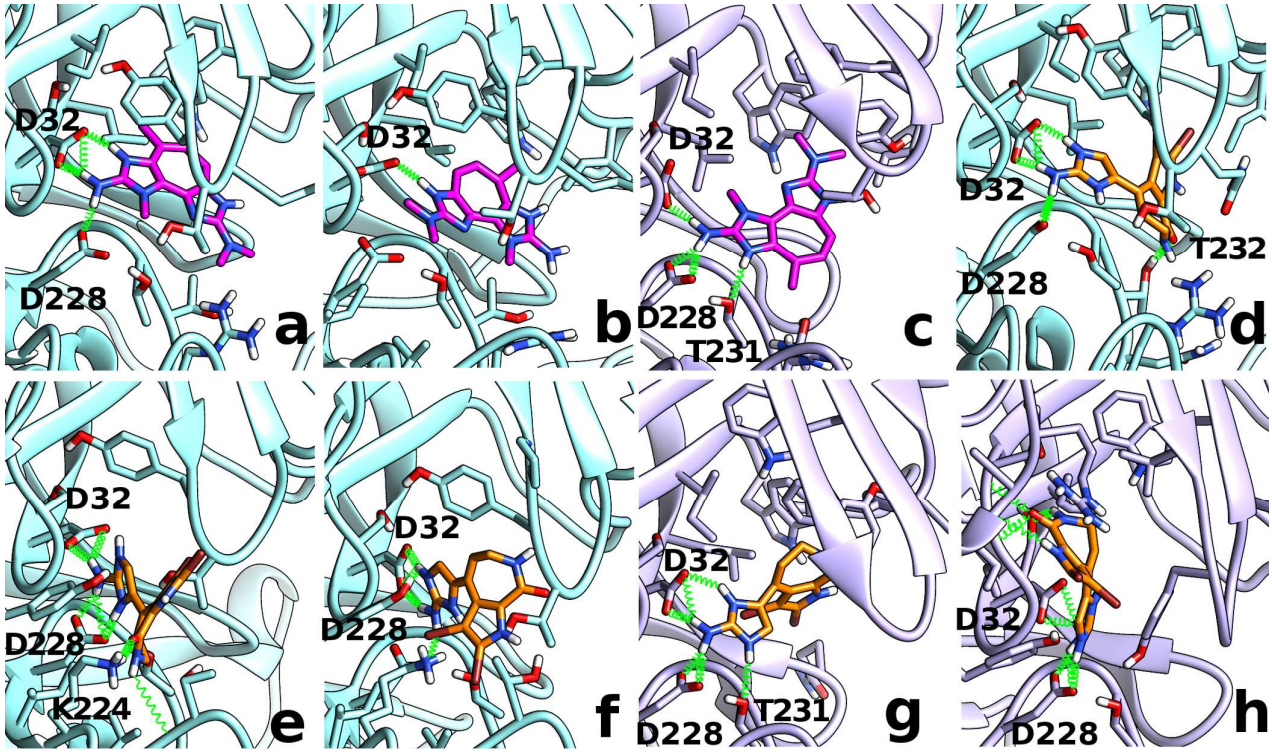

Figure 3. Representative 3D models of the hBACE-1 complexes with compounds 1 and 2. *The figure shows the same view of the ligand binding site region for the main selected poses after MD refinement: C1 (**a**), C2 (**b**) for complexes of the "closed" structure of hBACE-1 (cyan C atoms) with **1** (magenta C atoms), O2 (**c**) for complexes between the "open" structure of hBACE-1 (light violet C atoms) and **1**, C1 (**d**), C2 (**e**), C3 (**f**) for complexes of the "closed" structure of hBACE-1 with **2** (orange C atoms), O3 (**g**), O4 (**h**) for complexes between the "open" structure of hBACE-1 and **2**. Proteins are represented with ribbons plus stick sidechains for residues within 4 Å from the ligand and labels for the most relevant residues. A green spring represents stable ligand-protein H-bonds. H, N, O, S and Br atoms are painted white blue, red, yellow and red-brown, respectively.*

In C3 pose (**Figure 3f**) the bicyclic ring is external to the flap loop stacking against it, whereas the pyrrole ring and the 2-amino-imidazole group interact with Thr329 sidechain and both catalytic aspartate residues, respectively.

Six different poses, i.e. O1-O4 for **2**-p^- and O5-O6 for **2**-p^+, were selected from the docking runs carried out on the "open flap" form of the protein (PDB: 4ACU): O1, O2 and O5 poses lose their H-bonds with the catalytic aspartate residues during MD simulations, whereas O6 pose, exhibiting an estimated binding free energy above -7.0 kcal mol^{-1}, will not be discussed in detail.

In O3 pose (**Figure 3g**) the ligand is sandwiched between the catalytic site and the flap loop: the 2-amino-imidazole ring interacts with catalytic aspartate residues and Thr231; the polycyclic system interacts with Tyr71, Phe108 and Gln73. In O4 (**Figure 3h**) **2** also interacts with the flap loop, forming a π-stacking interaction with Tyr71 with the 2-amino-imidazole ring that in turn forms a stable network of HBs enforced by ionic interactions with the

catalytic aspartate residues and HB between the amide carbonyl and Ser36 backbone amide group, between its amide group NH and Ser35 sidechain and between the amino group of its pyrrole ring and the backbone carbonyl of Ile126. This pose exhibits the best estimated binding free energy of the set (-8.89±0.02 kcal mol^{-1}).

The binding modes of **1** and **2** show that the aminomidazole group is able to stably interact with both the catalytic aspartates and with the close Thr residue, recapitulating the binding already described for other inhibitors of this class, whereas the scaffold of both molecules interacts with the flap loop that actively contributes to the overall binding, with comparable energies, for these molecules.

***In vitro* mBACE-1 inhibition assay confirms modelling predictions for compounds 1 and 2 also on this target**

Human and murine BACE-1 share more than 95% sequence identity and the residues involved in interactions with both compounds are conserved. Thus mBACE-1 is a suitable system to validate the computational results on this target.

The inhibitory properties of the compounds on mBACE-1 activity was tested in the presence of different concentrations of **1** or **2**. The results reported in **Figure S2a** indicates that **1** exhibits a slightly higher inhibition power than **2**. The data, analyzed by a semi-logarithmic plot (**Figure S2b**) allow the determination of the inhibitor concentration required to get inhibition of half of the activity. The mean values of the IC_{50} calculated on the basis of four different experiments are reported in **Table 1**, showing similar IC_{50} values, in agreement with the comparable binding energy predicted for the two compounds.

Docking suggests possible interaction of compounds 1 and 2 with Aβ protofibrils

The available NMR solution structure (PDB:2BEG) of the protofibril (17–42) was used as target in docking studies to determine the potential ability of the two investigated compounds to form stable complexes with β-amyloid fibrils and/or their soluble precursors. Although the lack of a "canonical" binding site determines the spread of poses on a number of possible sites on the protofibril surface, two major aggregation of poses are observed for both ligands. Representative structures of these two binding modes are shown for **1** in **Figure 4a** (binding mode I) and **4-b** (binding mode II). Both modes are appreciably stabilised by both electrostatic and hydrophobic contributions. Looking at long-range electrostatic interactions, binding of **1** and **2** involves regions of the protein aggregate characterized by a large local negative electrostatic potential (red areas in **Figure 4a-b**). When considering specific interaction patterns, H-bonds reinforced by ionic interactions with Glu22 occur in both

modes, involving the less-substituted 2-amino-imidazole in **1** and the only amino-imidazole group in **2**. Cation-π interactions are found in both modes for **1**, between the more-substituted amino-imidazole ring and protein Phe20 (mode I, **Figure 4a**) or Phe19 (mode II, **Figure 4b**), and in mode II only for **2**, between the amino-imidazole group and Phe19. Mode I for **2** is instead stabilized by a weaker π-π interaction between ligand dibromo-pyrrole ring and Phe20. While exhibiting a similar pattern of interactions, the two poses differ essentially in the location of the binding site within the strand organization of the protofibril, since in mode I the ligand packs against the external face of the N-terminal β-sheet of the aggregate, whereas in II it points inside the internal space between the two sheets. Thus, both **1** and **2** exhibit favourite binding modes capable both of "patching" nascent sheets, and of disturbing the interactions in already-aggregated structures. In this view, these ligands can, in principle, both interfere with fibril formation, and destabilize existing fibrils.

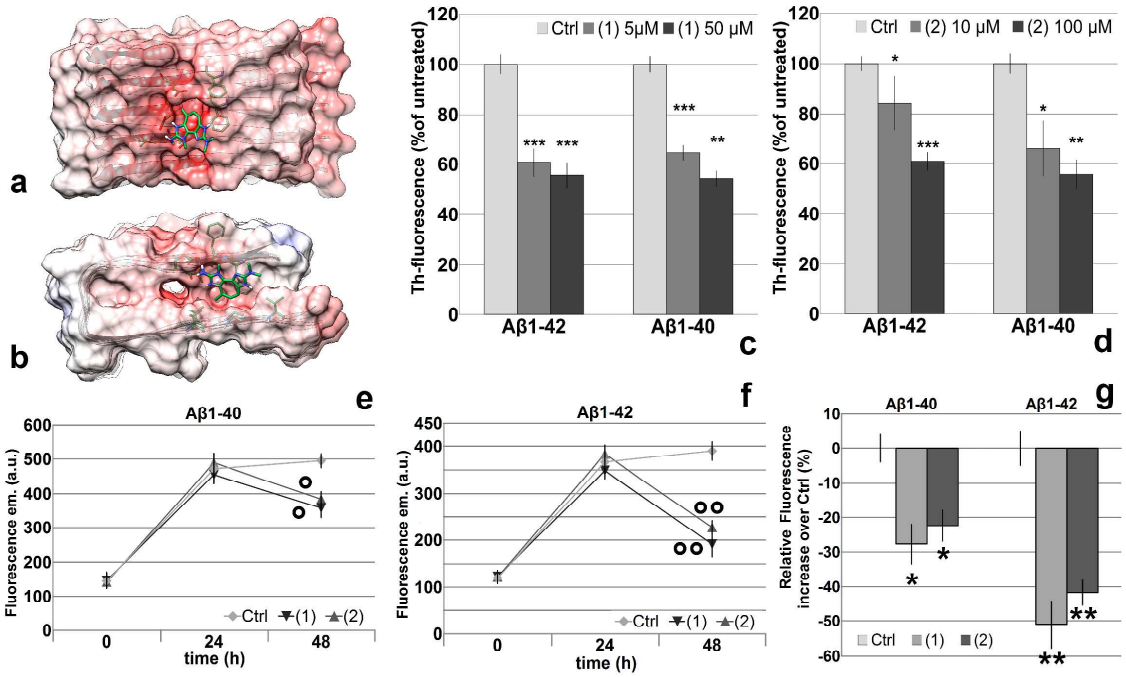

Figure 4. Prevention of $A\beta_{1-40}$ and $A\beta_{1-42}$ fibrillation and disruption of preformed fibrils by compounds 1 and 2. *Panels **a-b** shows representative poses from docking of **1** into the NMR structure (PDB:2BEG) of $A\beta_{17-42}$ protofibril. Proteins are represented with flat ribbons in a transparent surface painted according to APBS electrostatic potential, plus thin stick sidechains for residues within 4 Å from the ligand (thick stick). H, C, N and O atoms are painted white, green, blue and red, respectively. In panels **c-d** the effects of **1** (**c**) or **2** (**d**) on the fibrillation of Aβ peptides are measured by monitoring Th-T fluorescence emission. $A\beta_{1-40}$ and $A\beta_{1-42}$, (100 μM) incubated in 0.2M phosphate buffer, pH 8.0, in the presence of vehicle, **1** (5 and 50 μM) (**c**) and **2** (10 and 100 μM) (**d**) for 24 h at 37 °C. Data expressed as percentage of vehicle-treated samples (controls). Panels **e-g** shows the effects of **1** or **2** on the disruption of preformed fibrils. $A\beta_{1-40}$ and $A\beta_{1-42}$, (100 μM), were incubated in phosphate buffer at 37 °C; after 24 h, vehicle (DMSO), **1** (50 μM) or **2** (100 μM) was added into the buffer and the incubation was prolonged up to 48 h. For each condition of treatment, Th-T fluorescence for $A\beta_{1-40}$ (**e**) and $A\beta_{1-42}$ (**f**) was measured at 0, 24 (soon before drugs addition) and 48 h. Peptide fibrillation was measured after 48 h of incubation and expressed as relative increase (percentage) of Th-T fluorescence emission over the controls (**g**). All values represent the mean +/- SEM of three independent experiments. **c-d**: Statistical analysis was performed by ANOVA followed by Tukey post-hoc test: $p < 0.0001$ and $p<0.0003$ for $A\beta_{1-42}$ and $A\beta_{1-40}$; respectively, in panel **c** and $p < 0.001$ and $p<0.0047$ for $A\beta_{1-40}$ and $A\beta_{1-42}$; respectively, in panel **d**: *$p < 0.05$; **$p < 0.01$; ***$p < 0.001$ vs. controls. **e-g**: Statistical analysis was performed by two-tailed t-Student test: **e-f**: °$p < 0.05$; °°$p < 0.01$ vs. Th-T fluorescence at 24 hours in each set of treatment, **g**: *$p < 0.05$; **$p < 0.01$ vs. controls.*

Time-dependent fibrillation study of peptides $A\beta_{1-40}$ and $A\beta_{1-42}$ shows substantial completion of the process within 24 h

To test the effects of **1** and **2** on amyloid aggregation, first we evaluated the kinetics of $A\beta_{1-40}$ and $A\beta_{1-42}$ fibrillation by means of Th-T binding. **Figure S3a-b** in **Supporting Information** shows the spectra of Th-T fluorescence emission (460-560 nm) upon binding to $A\beta_{1-40}$ and $A\beta_{1-42}$ peptides, respectively. To establish a time-course of Aβ fibrillation, the assay was performed either immediately after dilution of the peptides or after 1, 5 and 24 h, and the intensity of Th-T fluorescence at 482 nm, representing the emission when the probe binds β-sheet structures[18], was calculated. **Figure S3c-b** depicts the kinetics of $A\beta_{1-40}$ and $A\beta_{1-42}$

fibrillation up to 72 h as fluorescence peak intensity at 482 nm. Although fibrillation of $A\beta_{1-42}$, as estimated from Th-T fluorescence, is much faster than that of $A\beta_{1-40}$, being already significant after 1 hour of incubation (see figures' insets), both peptides showed a sharp increase in fibrillation within 24 h of incubation, followed by steady slopes, indicating that the process is mostly completed after 24 h.

Compounds 1 and 2 prevent $A\beta_{1-40}$ and $A\beta_{1-42}$ fibrillation

To prevent the early phases of Aβ amyloidogenesis is nowadays regarded as a promising therapeutic strategy, since its represents a crucial step towards the formation of neurotoxic oligomers[19–22]. Thus, we evaluated the possibility that **1** and **2** could interfere with the fibrillation of $A\beta_{1-40}$ and $A\beta_{1-42}$ measured by Th-T fluorescence intensity. To this aim, we incubated both peptides (at the concentration of 100 μM) in phosphate buffer either in the absence or presence of **1** (5 and 50 μM, **Figure 4c**) or **2** (10 and 100 μM, **Figure 4d**). Both compound **1** and **2**, *per se* do not significantly interfere with ThT fluorescence (**Supplementary Figure S4**). ThT fluorescence intensity caused by $A\beta_{1-40}$ and $A\beta_{1-42}$ after 24 hours of incubation with both molecules, was compared to that produced in the absence of the drugs. Data plotted in **Figure 4** show that **1** at the concentration of 50 μM caused a significant inhibition of $A\beta_{1-40}$ and $A\beta_{1-42}$ fibrillation, evidenced by a 50% reduction of Th-T fluorescence increase. Compound **2** also reduced the fibrillation of both peptides, although its effect was less prominent as compared to **1**.

Compounds 1 and 2 revert $A\beta_{1-40}$ and $A\beta_{1-42}$ fibrillation

To further characterize the properties of **1** and **2** on Aβ amyloidogenesis, we investigated whether these compounds modify the intermolecular assembly of pre-aggregated amyloid peptides. In this experimental setting, $A\beta_{1-40}$ and $A\beta_{1-42}$ peptides were dissolved in phosphate buffer (t=0), induced to form fibrils for 24 h (t=24) and then incubated with **1** (50 μM) or **2** (100 μM); the assay was then prolonged for further 24 h in the presence or absence of the drugs (t=48). The amount of $A\beta_{1-40}$ and $A\beta_{1-42}$ fibrils was evaluated by monitoring Th-T fluorescence emission at t=0, 24h and 48h (**Figure 4e-f**). In control samples (treated with vehicle) at t 48, $A\beta_{1-40}$ and $A\beta_{1-42}$ continued a slow amyloidogenesis process, although starting to reach a plateau. The fibrillation of both peptides was affected by **1** and **2** as shown by the significant reduction of Th-T fluorescence emission observed at t=48h in comparison with control peptides, suggesting that the activity of these compounds is not limited to the early phases of Aβ amyloidogenesis but it is also significantly effective on preformed fibrils. Interestingly, $A\beta_{1-42}$ was more sensitive than $A\beta_{1-40}$: **1** inhibited $A\beta_{1-40}$ and $A\beta_{1-42}$ aggregation

of about 28 and 51%, respectively while **2** inhibited $A\beta_{1-40}$ and $A\beta_{1-42}$ fibrillation of about 22 and 42%, respectively (**Figure 4g**). Moreover, the intensity of Th-T fluorescence in the presence of $A\beta_{1-40}$ and $A\beta_{1-42}$ at t=48h was reduced when co-incubated with **1** and **2**, at lower levels than detected after 24 h of incubation (**Figure 4e-f**), indicating that the drugs are able to induce partial disaggregation of $A\beta_{1-40}$ and $A\beta_{1-42}$ complexes.

Atomic force microscopy assessment of the interference of compound 1 with $A\beta_{1-42}$ aggregation

Spectroscopic approaches provided a quantitative evidence of the interaction between Aβ (either 1-40 or 1-42) with (**1**) or (**2**) (see previous paragraphs). In order to clarify the underlying mechanism, the effect of (**1**) on $A\beta_{1-42}$ aggregation was analyzed using high resolution atomic force microscopy (AFM), which allowed a deeper insight into the interaction mechanism between $A\beta_{1-42}$ and (**1**). In **Figure 5a-c**, a typical aggregation kinetics of $A\beta_{1-42}$ is presented. This protein is initially monomeric, but after reconstitution in buffer solution it starts a well-studied aggregation process[23,24]. At the initial time, right after reconstitution, the sample appears mainly composed of small circular oligomers (**Figure 5a**) with a distribution of vertical size (height) clearly showing the presence of one peak at around 3 nm (see **Figure 5g**). After 24 hours of incubation, small oligomers have almost disappeared and the sample is organized in bundles of nodular fibers with a typical height of 7-10 nm. Finally, after 48h the size of fibrillary bundles grows and $A\beta_{1-42}$ organizes in an almost compact networked structure of fibers (**Figure 5c**). The aggregation mechanism in the presence of (**1**) is presented in **Figure 5d-f**. In particular, the initial time point, right after reconstitution is presented in **Figure 5d**, where the sample appears composed of small circular aggregates, similar to the corresponding condition without the substance (**1**) shown in **Figure 5a**. Nevertheless, a careful analysis of the size distribution of the small aggregates in the presence of (**1**), presented in **Figure 5g**, shows a pronounced bi-modal distribution, with one peak roughly corresponding to the one observed for $A\beta_{1-42}$ alone (around 3 nm) and a new one for smaller sizes, at about 1 nm. Moreover, the $A\beta_{1-42}$ aggregation kinetics at 24h and 48h is completely altered in the presence of (**1**). After 24h only few amorphous and compact aggregates are visible, on top of a feint network of disorganized material (**Figure 5e**). This trend is confirmed after 2 days (**Figure 5f**) where the surface is almost fully covered by a 1 nm-thick layer of proteins on top of which a population of small nm-sized globular aggregates is also present. This results demonstrate that, while soon after solubilization $A\beta_{1-42}$ has a very strong tendency to aggregate, forming oligomeric aggregates with a size of about 3 nm

(**Figure 5a,g**), substance (**1**) is able to interfere with this process, somewhat capping $A\beta_{1-42}$ molecules and preventing further aggregation. This mechanism result in the onset of a second population of smaller structures in the mix $A\beta_{1-42}$ + (**1**) (**Figure 5d,g**), together with some rapidly generated, putative $A\beta_{1-42}$ oligomers that partially avoided the action of (**1**). In the time course, this conflict between $A\beta_{1-42}$ tendency to self-aggregate and the action of (**1**) proceeds, so that no fibrillary structure is present after 24h, and after 48h any larger aggregate disappears, leaving a layer of small protein aggregates, possibly $A\beta_{1-42}$ + (**1**) structures. Interestingly, substance (**1**) was able to interfere not only with $A\beta_{1-42}$ oligomers, but also with mature fibers. In fact, a set of experiments was repeated by incubating a well formed $A\beta_{1-42}$ fibrillar structure (**Figure 5h**, after 24h of incubation, the same time point as in **Figure 5b**) with (**1**) for additional 24 hours and the result is shown in **Figure 5i**. The aggregation process of $A\beta_{1-42}$ is clearly blocked, with respect to the free aggregation resulting to the conformation depicted in **Figure 5c**, and also the aspect of the bundles is different, looking more amorphous and with less fibers. In this case, (**1**) interaction with $A\beta_{1-42}$ bundles forms a sort of capping layer around the fibers, possibly also altering the existing packing inside $A\beta_{1-42}$ agglomerates.

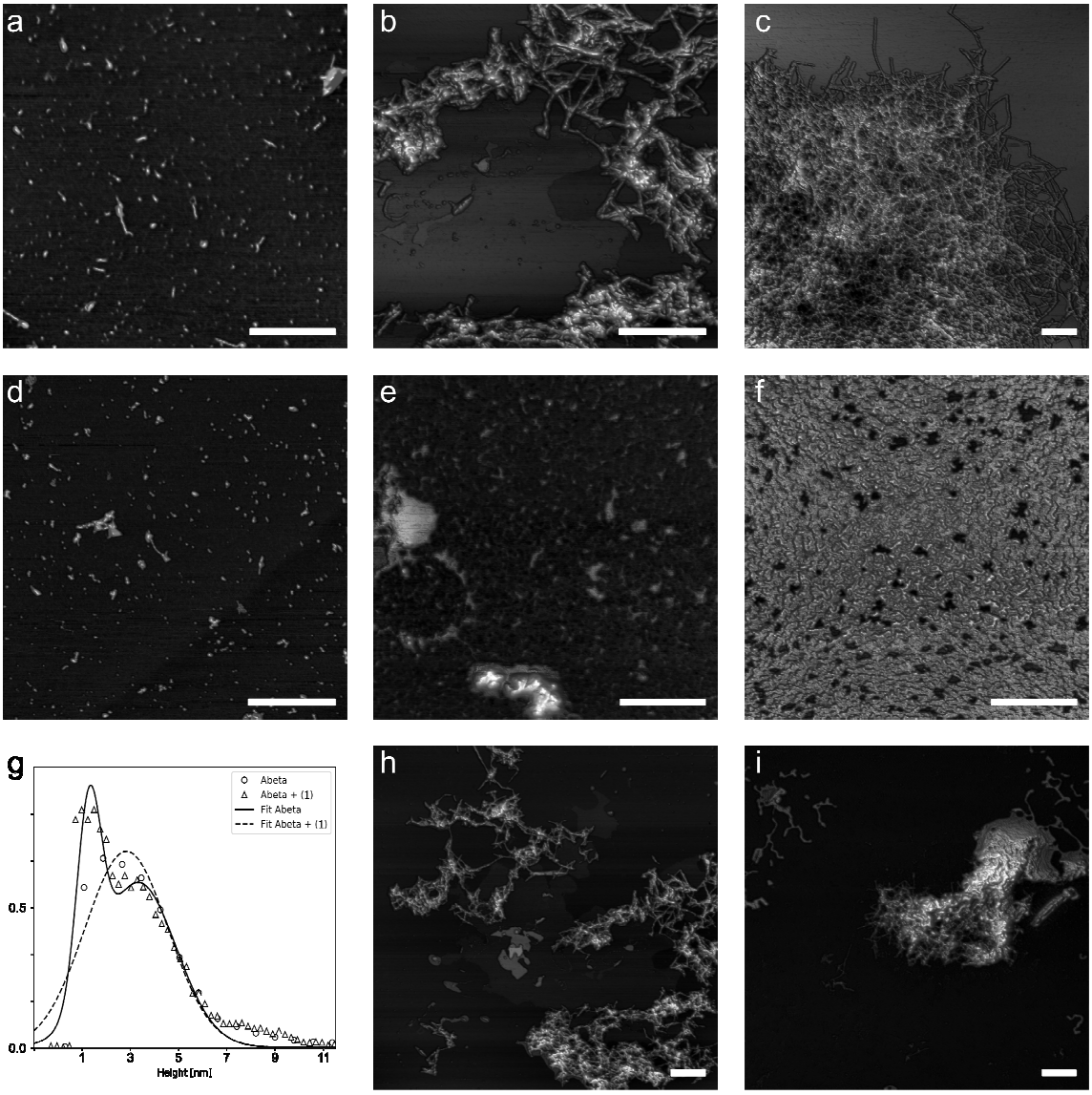

Figure 5: Atomic force microscopy analysis of the influence of (1) on Aβ aggregation. *The first row shows $A\beta_{1-42}$ 100 μM samples at the initial time (t=0, panel **a**), after 24h (**b**) and after 48h (**c**) of incubation at 37°C. Images of the second row represent $A\beta_{1-42}$ 100 μM samples incubated in presence of (**1**) at 100 μM and observed at the initial time (t=0, **d**), after 24h (**e**) and after 48h (**f**) of incubation at 37°C. The plot in panel **g** presents the height distribution of the proteinaceous features of $A\beta_{1-42}$ samples after 1h of incubation alone (circles) or after addition of (**1**) (triangles). The dashed line is a Gaussian fit of the height distribution for $A\beta_{1-42}$, centered at h=2.8 nm, while the solid line is the fit of the $A\beta_{1-42}$ + (**1**) distribution with a double Gaussian (centers in h_1=1.3 nm and h_2=3.3 nm). The last two images show the role of (**1**) on an already formed $A\beta_{1-42}$ sample: figure **h** is acquired after 24h of $A\beta_{1-42}$ incubation (the same sample as in **b**) and the image **i** was recorded after an additional 24h incubation in presence of (**1**). White bars correspond to 500 nm in all the panels.*

Compound 1 restores cortico-hippocampal functional connectivity after bilateral AMPA lesion of the nucleus basalis of Meynert

Encouraged by the *in vitro* results, a set of preliminary *in vivo* experiments was planned to evaluate the pharmacological effects of **1** on attention, learning, working and spatial memory, with respect to cortical and hippocampal electroencephalogram (EEG) theta rhythm during cognitive performance in an *in vivo* experimental model of AD already developed in our laboratories[25–30]. The study *in vivo* was limited to **1** since the available amount of **2** was too scarce for these experiments. In this disease model a selective excitotoxic lesion of the cholinergic terminals arising from the nucleus basalis of Meynert (NBM) to frontal cortex has been produced. By 3 weeks after AMPA injection, ChAT immunopositive neurons in bilateral NBM were markedly reduced to about 45% of the ChAT-positive cells content in the NBM of the unlesioned group (**Figure S5** in **Supporting Information**). In this regard, it is important to remark that no spontaneous recover of ChAT immunoreactive neurons was observed even after several weeks post-NBM lesions, in accordance with literature reports[31,32]. Compared to EEG of control animals (**Figure 6a**), NBM-lesioned animals showed increased theta power and *high voltage spindle* (HVS) in the cortex (**Figure 6b-c**), as well as a reduced theta rhythm oscillation in the hippocampus (**Figure 6e**). These EEG changes correlated with worse performance of lesion animals in learning and memory tasks assessed by the Morris water maze test (MWM) (**Figure 6f**). In rats with damaged NBM, the intracerebral (I.C.) injection (1 μl once daily for two weeks starting from surgery) of 1 μM **1** restored the physiological EEG pattern of theta range (4-7 Hz) both in neocortex and hippocampus (**Figure 6d-e**) and improved the cognitive performance in MWM (**Figure 6f**). In particular, **1** was able to restore the EEG architecture in lesioned animals, producing cortical desynchronization and significant reduction in theta power and HVS burst episodes in neocortex ($p<0.001$ *vs.* NBM-lesioned and saline-treated), while increasing firing in theta oscillation in hippocampus during spatial navigation improving attention/working memory. In the present experimental model of AD, EEG events were unequivocally related to cognitive deficit. The present preliminary data suggest that **1** is able to restore cholinergic cortico-hippocampal functional connectivity.

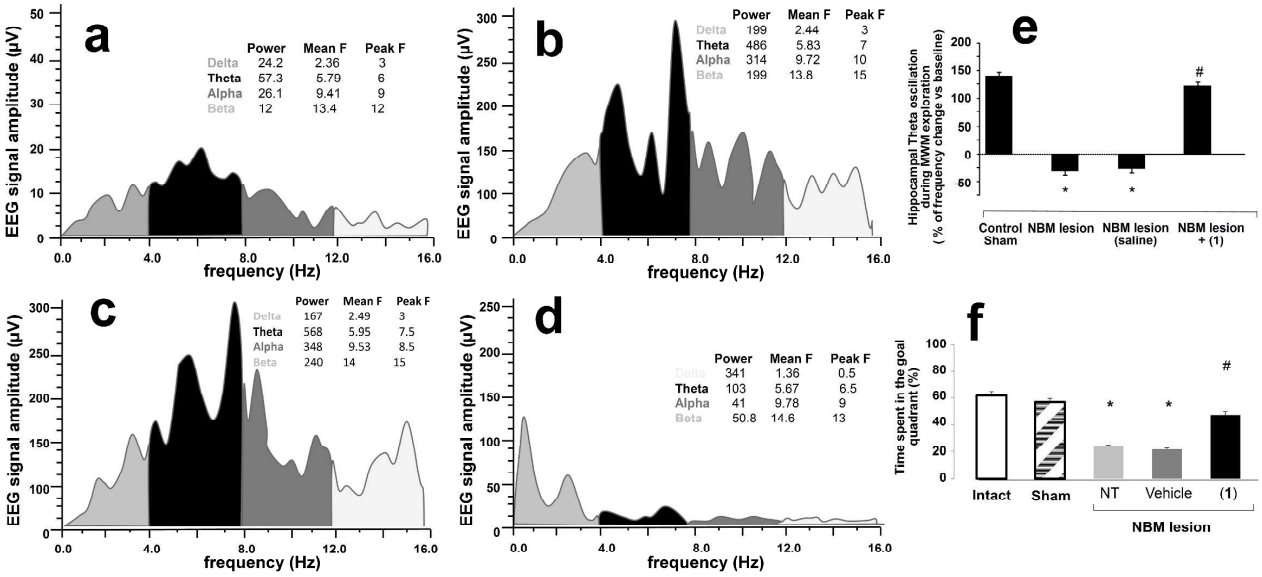

Figure 6. Effects on neocortical and hippocampal EEG activity and in Morris water maze (MWM) of treatment with compound 1 in NBM-lesioned rat. *Panels **a-d** show the time courses of the EEG power for sham-operated (**a**), lesioned untreated (**b**), lesioned vehicle-treated (**c**), lesioned treated with 1 μM **1** (1 μL ic) (**d**). Note the significant increase in EEG power in the theta range (**b** and **c**) in lesioned animals. The complete restore of normal EEG architecture and EEG power following treatment with **1** is also here depicted. EEG tracing was recorded on fronto-parietal neocortex of both hemispheres (n = 7 for each group). Since no significant change in EEG cortical activity was recorded in both control groups (intact and sham), in panel **a** both control group are depicted in a single EEG spectrum. Histogram in panel **e** shows the changes in hippocampal theta activity (frequency in theta oscillations) during exploration in MWM in control (intact and sham) and in experimental groups (n = 7 for each group). Hippocampal theta oscillation was directly recorded in CA1 area. Note the restored mean theta oscillations frequency in NBM-lesioned animals after treatment with **1**. Data are expressed as percent change (mean ± SEM). *p < 0.0001 versus intact and sham-operated groups; $^{\#}$p < 0.0001 versus NBM-lesioned not treated and NBM-lesioned saline-treated groups. No significant change in hippocampal activity was recorded between the both control group (intact and sham). Seven rats were used for each experiment. Panel **f** shows the spatial memory performance of NBM-lesioned animals in swim paths in the Morris water maze (MWM) and in target-hidden platform. NBM-lesioned rats showed a significant reduction in time spent in the goal quadrant in each daily session. Rats treated with the active dose of **1** showed a significant increase in the time spent in the goal quadrant. n = 7 for each group. Data expressed as mean ± SEM. *p < 0.001 versus control groups; $^{\#}$p < 0.01 versus lesioned groups. Statistical analysis of the data was performed: a) for EEG: on the EEG signal amplitude (μV), comparing each group with controls by analysis of variance (ANOVA) followed, if significant, by the post-hoc Tukey-Kramer test for multiple comparisons; b) for MWM: by two-way ANOVA with repeated measures for latency values (calculated as mean latency periods) (comparing group by group, day by day trials and difference between trial 1 and trial 2 for the 5 consecutive days) and by t-student test for unpaired samples for the time spent in the target quadrant (swimming 60 s without platform) in the probe performance.*

CONCLUSIONS

The previous discovery of the AChE-inhibiting activity of a pseudozoanthoxanthin prompted us to search the ICB-CNR natural products collection for compounds featuring similar functional groups. This search identifies two molecules, compound **1**, an analog of the template pseudozoanthoxanthin, and stevensine (compound **2**), used in a virtual screening study on selected molecular targets relevant for AD. In particular, on the basis of structural features of the investigated compounds, including a positively charged (poly)aromatic

scaffold, we have focused our attention on targets sharing similar pharmacophore profiles, i.e. both the acetyl/butyryl-cholinesterase and β-secretase 1 enzymes. The results of the computational study are confirmed by biochemical data, which shows that compound **1** is active on all the tested targets, in the micromolar (AChE, BuChE) or low-micromolar (BACE-1) range. Compound **2**, while exhibiting activities on AChE and BACE-1 comparable to those of **1**, is, as predicted, less active (by an order of magnitude) on BuChE.

Differences in activity of **1** vs. **2** on AChE suggest the occurrence of an "internal decoy" effect that could affect, in general, those ligands capable of binding with comparable affinity both CAS and PAS sites of AChE.

Predicted BACE-1 inhibition mode for both **1** and **2** recalls that described for other known aminomidazole-based inhibitors as for the contact pattern with enzyme catalytic residues, and also feature additional interactions with the protein flap loop. The comparable predicted binding energy between the compounds is fully confirmed by the IC_{50} values obtained from biochemical assays.

Furthermore, both compounds are also predicted to bind Aβ-fibrils. Both Th-T fluorescence and AFM experiments demonstrate that the two compounds affect fibrillation and aggregation of $A\beta_{1\text{-}40}$ and $A\beta_{1\text{-}42}$, reducing and reverting fibrillation and favouring amorphous aggregates, **1** resulting more effective than **2** in all activities.

However, compound **1** also provides encouraging results in *in vivo* experiments (available amounts of **2** presently prevents *in vivo* test). In particular, compound **1** is able to revert EEC and cognitive alterations induced by NBM excitoxicity, thus recovering the cortico-hippocampal functional connectivity in mice, and prompting us to continue the pharmacological characterization of this molecule as a potential anti-neurodegenerative drug and the possible extension of the study to new related compounds.

In particular, the "one/two-aromatic ring + 2-amino-imidazole" scaffold has emerged as a promising template to search natural or design synthetic new multiligands for the drug targets of relevance to Alzheimer's disease treated in the present study.

MATERIAL AND METHODS

Computational Methods

Docking

Docking studies were performed with AUTODOCK 4.2[33]. The crystallographic structures of human AChE (hAChE) and human BuChE (hBuChE) (PDB: 4EY6 and PDB: 4BDS, respectively), two structures for human BACE-1 (hBACE-1), representative of the flap open

(PDB: 4ACU) or closed (PDB: 2QZL) and the β-amyloid protofibril (17–42) NMR structure (PDB: 2BEG), along with the ligands, were processed with AutoDock Tools (ADT) package version 1.5.6rc1[33] to merge non polar hydrogens and calculate Gasteiger charges. Grids for docking evaluation with a spacing of 0.375 Å and 70x70x70 points for hAChE and 60x60x60 points for hBuChE and hBACE-1, centered in the ligand binding pocket, were generated using the program AutoGrid 4.2 included in Autodock 4.2 distribution. In the case of protofibril (17–42), a uniform sampling of the whole fibril model was obtained by applying six partially overlapping 70x70x70 point grids with a spacing of 0.375Å, corresponding to 26.25 Å x 26.25 Å x 26.25 Å regions.

Selected residues of protein targets were allowed rotatable and in particular Tyr76 and Gln78 for 4ACU, Gln78 and Thr77 for 2QZL, and Glu292, Ty337, Tyr341 and Asp74 for 4EY6. Lamarckian Genetic Algorithm (LGA) was adopted to perform molecular docking along with the following docking parameters: 100 individuals in a population with a maximum of 15 million energy evaluations and a maximum of 37000 generations, followed by 300 iterations of Solis and Wets local search. A total of 100 docking runs were performed for each calculation. For each ligand, the selection criteria for the best poses was the most favorable binding energy and the cluster population. In the case of fibrils, the poses endowed with the best binding energy were selected from each docking run and compared among each other by visual inspection to obtain the representative binding modes for each protein region.

Ligand parametrization

Ligand geometries were fully optimized using GAMESS program[34] at the Hartree-Fock level with STO-3G basis set. The partial atomic charges for the ligands were derived using the RESP procedure of restrained fit to the HF/6-31G*/STO-3G electrostatic potential[35].

Loop modelling

The loops missing in the crystallographic structures used in this study were modelled with MODELLER v9.11 program[36].

Molecular dynamics

Representative complexes for each ligand were completed by addition of all hydrogen atoms and underwent energy minimisation and then molecular dynamics (MD) simulations with pmemd.cuda module of Amber12 package[37], using ff12SB force field[37] for the protein and gaff parameters[38] for the ligands.

To perform molecular dynamics (MD) simulation in solvent, each complex was confined in water boxes using tleap module of AmberTools12 program [8] with a minimum distance between solute and box surfaces of 10 Å, filled with TIP3P water molecules and counterions

(Na^+) to neutralize the system. The solvated systems were then energy minimized through 1000 steps with solute atoms restrained to their starting positions using a force constant of 10 kcal $mol^{-1}Å^{-1}$ prior to MD simulations. After this, the molecules underwent 90 ps at 300K (constant NVT ensemble) with positional restraints on solute atoms of 5 kcal $mol^{-1}Å^{-1}$, followed by 60 ps (constant NPT ensemble), using the same constant force on positional restraints. Production runs were carried out at constant temperature (300 K) and pressure (1 atm) for 10 ns up to 30 ns with a time-step of 2 fs. Langevin dynamics with a collision frequency of 5 ps^{-1}. Bonds involving hydrogens were constrained using the SHAKE algorithm[39]. Particle Mesh Ewald method was used to evaluate electrostatic interactions with a cutoff of 10.0 Å; the same cutoff was used for van der Waals interactions.

Molecular Graphics and electrostatic potential analysis

Protein and complex electrostatic potential have been calculated with APBS 1.5 program[40]. Graphic analysis and molecular structure plotting have been performed with UCSF Chimera 1.12 software[41].

Isolation, purification and characterization of Compounds 1 and 2

Isolation and purification of Compound 1

Compound **1** was isolated from an unidentified Caribbean coral which was collected by Scuba diving in Mexico along the coast of Cancùn during January 1997. After collection the biological material was immediately frozen at -20 °C and transferred to the ICB-CNR laboratories where it was stored at -20 °C until the extraction with acetone. The acetone extract was portioned between diethyl ether, *n*-butanol, and water, and the resulting three fractions were analyzed by both TLC chromatography and ^{1}H NMR. The butanolic fraction was fractionated on a Sephadex LH20 chromatography column eluted with a mixture of chloroform/methanol (ratio 1:1) yielding a main fluorescent fraction (20.0 mg). The latter was then purified on preparative TLC (Merck Kieselgel 60 F254, 0.5 mm, $CHCl_3/CH_3OH$, 7:3) to obtain pure compound **1** (12.0 mg) which was identified by NMR spectroscopy and mass spectrometry (purity 95%). Compound **1** was previously reported from a deep water Pacific zoanthid *Gerardia* sp.[42].

Characterization of Compound 1

^{1}H NMR (CD_3OD, Bruker 400 MHz) δ 7.78 (1H, d, J = 10 Hz, H-7), 7.67 (1H, d, J = 10 Hz, H-8), 4.38 (3H, s, H_3-11), 3.38 (6H, s, H_3-12 and H_3-13), 2.82 (3H, s, H_3-10); ^{13}C NMR (Indirect detection from HSQC and HMBC, CD_3OD, Bruker 400 MHz) δ 167.2 (s, C-5), 159.3 (s, C-2), 153.2 (s, C-4a), 151.4 (s, C-9), 147.7 (s, C-6a), 136.8 (s, C-9a), 132.3 (s, C-

3a), 131.3 (d, C-8), 118.9 (d, C-7), 38.0 (q, C-12 and C-13), 33.0 (q, C-11), 23.4 (q, C-10). LR-ESIMS *m/z* 257 $[M+H]^+$; HR-ESIMS *m/z* 257.1520 $[M+H]^+$ (calcd. for $C_{13}H_{17}N_6$ 257.1515).

Isolation and purification of Compound 2

Compound **2** was recovered from the sponge *Axinella verrucosa* collected by Scuba diving in the Gulf of Naples in October 2008. After collection the sponge was kept frozen at -20°C until extraction with acetone. The butanolic soluble portion of acetone extract was subjected to a Sephadex LH20 chromatography (chloroform/methanol, 1:1) yielding two main fraction containing stevensin (**2**) by ^{1}H NMR. These fractions (20.0 mg and 9.0 mg) were further purified by HPLC on a semipreparative RP-amide column eluted with a 35 minutes gradient from 40% to 100% of methanol in water with 0.1% of TFA (flow 1.5 mL/min) obtaining 5.0 mg of pure stevensine (**2**) (purity 98%) identified by comparison NMR and mass data with literature[43].

Characterization of Compound 2

^{1}H NMR (CD_3OD, Bruker 600 MHz) δ 6.85 (1H, s, H-15), 6.30 (1H, dd, *J* = 7 and 7 Hz, H-9), 3.62 (2H, d, *J* = 7 Hz, H_2-8); selected ^{13}C NMR ((Indirect detection from HSQC and HMBC, CD_3OD, Bruker 600 MHz) δ 164.1 (s, C-6), 149.2 (s, C-13), 128.2 (s, C-5),127.2 (d, C-9 and C-11), 123.3 (s, C-4), 112.7 (d, C-15), 38.9 (t, C-8); LR-ESIMS *m/z* 386 $[M+H]^+$; HR-ESIMS *m/z* 385.9259 $[M+H]^+$ (calcd. for $C_{11}H_{10}{}^{79}Br_2N_5O$ 385.9252).

Enzymatic assays

AChE and BuChE activity

Acetylcholinesterase from human erythrocytes (hAChE), butyrylcholinesterase from equine serum (eqBuChE), acetylthiocholine, butyrylthiocholine, 5',5'-dithiobis-2-nitrobenzoic acid (DTNB), were purchased from Sigma-Aldrich (Milan, Italy). Cholinesterase activity was assayed by the Elmann method[44] using acetylthiocholine or butyrylthiocoline as substrate for hAChE or eqBuChE, respectively. The reduction of dithiobisnitrobenzoate by the thiocholine, produced by the enzymatic hydrolysis of thiolated substrates, was followed colorimetrically (412 nm) at room temperature (22-25 °C). The reaction mixture (500 µL) contained 330 µM DTNB and the appropriate amount of substrate, in 0.1 M sodium phosphate buffer, pH 7.1. The reaction was started by the addition of 100 mU/mL or 200 mU/mL of hAChE or eqBuChE, respectively, and the initial rate of the reaction was derived from the linear portion of the kinetics.

The concentration of inhibitor required to reduce the enzymatic activity to 50% (IC_{50}) was derived from semi-logarithmic plots in which the residual cholinesterase activity was

determined at different concentrations of inhibitor, using a thiolated substrate concentration of 500 μM. Linear curve fits were obtained with the least-squares method, and the significance of the correlation was estimated from the squared correlation coefficient r^2, which was always higher than 0.95.

The kinetic parameters of the enzymatic reaction K_m and V_{max}, were derived from the determination of the enzyme activity at 6 different acetylthiocholine or butyrylthiocholine concentrations (80 – 500 μM) chosen in order to give similar weights in the regression. Data were either interpolated in the Michaelis-Menten equation or treated with the Lineweaver-Burk equation, giving similar results.

The inhibition constant K_i was derived from Dixon plots[45] or determined by measuring the kinetic parameters in the presence of different inhibitor concentrations, 0.2 – 30 μM for AChE or 3 – 100 μM for BuChE. The values of K_i were derived either from Dixon plots, or from the equation $V_{max}' = V_{max} / (1 + [I]/K_i)$, where V_{max}' is the V_{max} value measured at the [I] concentration of inhibitor. They represent the mean of at least 8 different determinations. The statistical significance of the mean values obtained was evaluated by the *t* probability value in a single group t-Student test.

BACE-1 activity

The fluorescent peptide substrate containing the Lys-Met/Asn-Leu aminoacid substitution of the amyloid precursor protein (APP) β-secretase cleavage site, was purchased from Sigma-Aldrich. Mouse BACE-1 (mBACE-1) (recombinant) and BACE-1 Inhibitor I, were from Life Technology. BACE-1 inhibitor IV solution (10 mM in DMSO) was from Calbiochem. mBACE-1 activity was assayed by a fluorimetric method[8,46] using the Enspire™ Multimode Plate Reader (Perkin-Elmer) in the kinetic Fluorescence method. The assays were performed in black polystyrene 96-well microtiter plates. The reaction mixtures, contained 2.1 ng/μL mBACE-1 in 50 mM ammonium acetate buffer, pH 4.5 supplemented with 1 mM triton X-100, and the appropriate amount of the inhibitor. The mixture was incubated for 10 min at room temperature (22-25 °C) and the reaction started by adding 100 nM final concentration of the fluorescent peptide substrate of which above, and was followed kinetically up to 120 min. The enzymatic peptide cleavage led to the appearance of a fluorescence signal using excitation and emission wavelength of 320 and 420 nm, respectively. The rate was derived from the linear portion of the kinetics, usually in the first 30 min of the reaction. The concentration of inhibitor required to reduce the enzymatic activity to 50% (IC_{50}) was derived from semi-logarithmic plots in which the residual mBACE-1 activity was determined at

different concentrations of inhibitor. Linear curve fits were obtained with the least-squares method, and the significance of the correlation was estimated from the squared correlation coefficient r^2, which was always higher than 0.95.

Characterization of $A\beta_{1-40}$ and $A\beta_{1-42}$ aggregation

$A\beta_{1-40}$ and $A\beta_{1-42}$ aggregation

Human $A\beta_{1-40}$ and $A\beta_{1-42}$ were purchased by Anaspec (Fremont, Ca, USA). Thioflavin T was purchased by Sigma-Aldrich (Milan, Italy). Peptides were dissolved in 0.2 M phosphate buffer pH 8.0 to reach working concentration of 100 μM; 50 μL of solution were incubated r. t. for 24 h at 37 °C[47]. When specified, **1** and **2** were present in the aggregation buffer.

Disruption of pre-aggregated $A\beta_{1-40}$ and $A\beta_{1-42}$

Peptides aggregation was induced as above described; then, **1** and **2** were added and incubation was prolonged for additional 24 hours. $A\beta_{1-40}$ and $A\beta_{1-42}$ aggregation was measured by thioflavin-T (Th-T) binding assay (see below) at the beginning of incubation, immediately before **1** or **2** treatment, and 24 h after the addition of each drugs.

Thioflavin-T (Th-T) binding

To measure peptide aggregation, 50 μL of test solution was added to 450 μL of Th-T 10 μM (dissolved in 50 mM Glycine-NaOH buffer, pH 8.5), gently mixed for 1 min, and read with Luminescence Spectrometer LS50B (Perkin Elmer). Emission spectra between 460 and 490 nm were collected upon excitation at 450 nm[48].

Atomic Force Microscopy (AFM)

AFM analysis was carried out on Aβ1-42 preparations aggregated at a monomer concentration of 100 μM, either in the presence or in the absence of vehicle two molecules at 100 μM concentration for a maximum of 48h [see previous sections for detailed description of the treatment conditions]. Aβ samples were imaged as previously described[49]]. Before imaging, all samples were diluted 50 times in PBS and were immediately spotted on freshly cleaved mica supports (Agar Scientific, USA), at a final concentration of 2 μM. After an incubation of 3 min, the samples were washed with ultrapure water and dried under a gentle nitrogen stream. AFM experiments were performed by using a Multimode AFM head (Bruker, USA), equipped with an E piezo-scanner. Images were acquired in tapping mode, in air. Single beam uncoated silicon cantilevers (OMCL-AC160TS, Olympus, Japan) with a nominal resonance frequency of 300 kHz and typical tip radius of curvature of 10 nm were used. Data analysis

and image processing were performed using the free software Gwyddion[50]. All images were flattened by subtracting the best plane (for images smaller than 1 μm) or the best sphere (for larger images) and filtered to remove scars.

Analysis of data

The extent of peptide aggregation was determined by Th-T binding and measured as the maximum intensity of Th-T fluorescence at 482 nm. Data were expressed as percent of Th-T binding in the presence of drugs, compared to the aggregation in the absence of treatment.

***In vivo* experimental design and procedures**

General features

A set of experiments was carried out to appraise the ability of **1** to revert disrupted neocortical and hippocampal EEG activities, as well as cognitive functions, in NBM damaged rats. Short term treatment with 1 μM **1** (1 μL for two weeks intracerebrally in the same area), in rats bilaterally lesioned at NBM by AMPA, started the same day of surgery. Furthermore, behavioral tasks for assessing attention and memory performance were performed. Each experimental group consisted of seven rats.

Drugs

2-Amino-3-(3-hydroxy-5-methylisoxazol-4-yl)propionic acid (AMPA) hydrobromide, were purchased from Tocris (Avonmouth, UK). Choline-acetyltransferase (ChAT) monoclonal antibodies were purchased from Boerhringer (Mannheim, Germany). All other chemical and biological reagents and solvents used were purchase from Sigma-Aldrich Company.

Animals

Male Wistar 3-months young rats (weighing 200–250 g), purchased from Charles River Laboratories, Italy, were used in the experiments. Animals were group-housed (12 h light/dark cycle) with *ad libitum* access to food and water. All animals were treated under standard conditions, according to the guidelines for care and use of experimental animals of the European Community Council directive (86/609/EEC). The experimental protocol and procedures were also approved by the Italian Ministry of Health.

Surgery

In anesthetized rats with chloral hydrate (400 mg/kg, i.p.), bilateral lesion of the NBM was stereotaxically performed (brain coordinates: AP: −0.9 from bregma; L: 2.6;V: 7.4 from skull), according to the atlas of Paxinos and Watson and by intracerebral infusion of

excitotoxic AMPA (1.3 μg/0.5 μL), using a Hamilton syringe through a Teflon tube connected by an injector (26 gauge, rate of microinfusion 0.1 μL/min). To permit the recording of theta activity in the hippocampus, a bipolar recording electrode was positioned into the CA1 area according to the atlas coordinate of rat brain. No AMPA was injected into the sham-operated rats. After surgery, all the animals were housed for 2 weeks before using for EEG and behavioural tests.

Electroencephalography (EEG)

Electroencephalograms were recorded in lesioned animals two weeks after the surgery. Changes in neocortical and hippocampal theta rhythm were monitored during behavioral tasks. EEG signal, derived from neocortical activity (ranging 0.25 to 16 Hz) as well as hippocampal theta rhythm (4–7 Hz), was amplified (set at 0.3 Hz and 10 kHz) and digitized and it was continuously monitored and recorded by a computerized apparatus (Galileo Vega 24. ESA-OTE Biomedica, Florence, Italy). For statistical purpose, bipolar signals, derived from each neocortical area in both brain hemispheres as well as in the hippocampus, were analyzed. Quantitative EEG (qEEG) analysis was performed on the theta range in the hippocampus as well as on the whole EEG spectrum in the cerebral cortex. Five artifact-free epochs, of 10 s each, selected from electroencephalogram baseline and that recorded during the performance in behavioral tasks, were processed using Fast Fourier Transform as previously described[25]. Statistical analysis of the data was performed on the EEG signal amplitude (μV), comparing each group with controls by analysis of variance (ANOVA) followed, if significant, by the *post-hoc* Tukey-Kramer test for multiple comparisons. In each group, the baseline EEG activity versus EEG recording during the behavioral performance was evaluated.

Morris Water Maze (MWM)

The spatial memory ability in rats was assessed by Morris water maze (MWM) apparatus[51], consisting of a swimming pool (diameter 150 cm, height 50 cm) which was filled with cloudy water at room temperature to a depth of 30 cm. The pool was ideally divided into four quadrants of equal area and a glassy, transparent platform (diameter 15 cm), hidden 1 cm below the water surface, was placed midway between of one quadrant and its location changed every day. The rat was introduced into the pool in the opposite quadrant and the time taken to reach the escape platform was measured. If animal failed to do so within 180 s, it was placed on the platform for 20 s and then placed in the home cage.

The rat was subjected to two daily trials for 5 consecutive days with an inter-trial interval of

15 min. The point of entry of the rat in the pool and the location of the escape platform remained unchanged between trial 1 and trial 2 but was changed on each day. Some visual cues were located in the room to facilitate the rat strategy in navigation to target platform. The decrease in escape latency from day to day in trial 1 represents reference long-term memory while that from trial 1 to 2 is consistent with working, or short-term memory. Lesioned animals were trained to find the hidden platform two weeks after surgery. A probe trial, consisting in a trial in which animals swam in the pool without platform, was performed on the fifth day. The percentage of time spent in the target quadrant around the previous platform location, during the probe trial, represent the spatial reference memory. Two-way ANOVA with repeated measures was used to analyze latency values calculated as mean latency periods (comparing group by group, day by day trials and difference between trial 1 and trial 2 for the 5 consecutive days). Whereas the time spent in the target quadrant (swimming 60 s without platform) in the probe performance was calculated by *t*-student test for unpaired samples.

Immunohistochemistry

Brain content of ChAT immunoreactive neurons was determined to assess the changes in this cholinergic marker after the bilateral lesion of NBM. In this regard, it is to stress the fact that no spontaneous recovering of ChAT immunoreactive neurons has been found, not even after several weeks post NBM lesion, in accordance with literature reports[31,32]. In brief, rats were perfused with 50 mL cold phosphate-buffered saline (PBS), followed by 200 mL of 4% paraformaldehyde solution in 0.1M phosphate buffer (pH 7.4). Brains were then removed and postfixed in the latter solution overnight, followed by 20% sucrose solution in PBS for 24 h. The brains were then mounted on the freezing microtome and 30µm-thick sections of both the NBM were cut and processed for ChAT immunohistochemistry. The free-floating sections were first rinsed in PBS and then left overnight in ChAT monoclonal antibody in 0.20% Triton-X-100 and incubated at 4 ◦C for 24 h. The primary antibody was then removed and the sections exposed to the secondary antibody, biotinylated antirat immunoglobulin (lgG), and then to avidin-biotin-horseradish peroxidase, followed by diaminobenzidine. Antibodies were used at the concentration of 1:1000. Stained sections were then examined. Quantitative analysis of ChAT-positive neurons in both the NBM was carried out using a computerized image analysis system (Axiophot Zeiss microscope equipped with a Vidas Kontron system). The total number of stained cells in three consecutive sections was divided by the total area considered, to obtain the total number of ChAT-positive cells per mm^2. To quantify the neuronal loss, analysis of variance (ANOVA) with repeated measures followed, if significant,

by the post-hoc Tukey-Kramer test for multiple comparisons was used.

ASSOCIATED CONTENTS

Supporting Information

Main interactions and calculated binding free energy in models of the AChE/BuChE (**Table S1**) and BACE-1 (**Table S2**) complexes with compounds **1** and **2**; dose-dependent inhibition profile of **1** and **2** on AChE or BuChE (**Figure S1**) and BACE-1 (**Figure S2**); time-dependent aggregation of $A\beta_{1\text{-}40}$ and $A\beta_{1\text{-}42}$ (**Figure S3**); Thioflavin-T fluorescence emission spectra (Figure S4); ChAT immunostaining to show the neuronal loss in NBM after focal infusion of AMPA (1.3 μg/0.5 μL) (**Figure S5**).

AUTHOR INFORMATION

Corresponding Author

* E-mail: pamodeo@icb.cnr.it

ORCID

Rosa Maria Vitale: 0000-0001-9243-1307
Vincenzo Rispoli: 0000-0003-3433-6736
Stefano Thellung: 0000-0002-2010-331X
Marianna Carbone: 0000-0003-3729-5714
Maria Letizia Ciavatta: 0000-0002-7308-1011
Ernesto Mollo: 0000-0001-7379-1788
Rosaria Arcone: 0000-0002-8507-4361
Margherita Gavagnin Capoggiani: 0000-0002-9532-4555
Mariorosario Masullo: 0000-0003-4485-7383
Tullio Florio: 0000-0002-2394-996X
Pietro Amodeo: 0000-0002-6439-7575

Author Contributions

P.A., R.M.V. and V.R. designed the study. P.A. and R.M.V. designed and carried out molecular docking and dynamics studies and computational/molecular graphic analysis. V.F. contributed to molecular docking studies. M.C., M.L.C., E.M. and M.G. designed and carried out extraction, purification and characterization of compounds. M.M. and R.A. designed the cholinesterase/BACE-1 inhibition assays. D.D. and R.S. performed the cholinesterase/BACE-1 inhibition assays. T.F. designed Aβ aggregation inhibition studies. S.T. performed Aβ aggregation inhibition studies. V.R. designed and performed *in vivo* tests. P.A. and R.M.V. wrote the manuscript. T.F., M.G., M.M., R.A. and V.R. contributed to write the manuscript. All authors read and approved the final manuscript.

Funding

This research work was supported by a grant from MIUR-ITALY PRIN2015 "*Top-down and bottom-up approach in the development of new bioactive chemical entities inspired on natural products sca□olds*" (Project No. 2015MSCKCE_003) to M.G. and M.L.C., by Alzheimer's Association Grant NIRG-14-321500 to T.F. and by the University of Naples "Parthenope", "*Bando per la ricerca individuale*" to M.M. and R.A.

Notes

The authors declare no competing financial interest.

ACKNOWLEDGEMENTS

P.A. and R.M.V. acknowledge Mr Salvatore Donadio for technical assistance in database development and management.

ABBREVIATIONS

Aβ, β-amyloid peptide; AD, Alzheimer's disease; ACh, acetylcholine; AChE, acetylcholinesterase; AChEI, acetylcholinesterase inhibitors; AMPA, 2-Amino-3-(3-hydroxy-5-methylisoxazol-4-yl)propionic acid; BuChE, butyrylcholinesterase; BuChEI, butyrylcholinesterase inhibitors; BACE-1, β-secretase; CAS, catalytic anionic site; ChAT, choline-acetyltransferase; DTNB, 5',5'-dithiobis-2-nitrobenzoic acid; EEG, electroencephalogram; HB, hydrogen bond; H-NH_2-Im, 2-amino-imidazole ring; H-NMe_2-Im, 2-N',N'-dimethylamino-imidazole ring; MD, molecular dynamics; Me-NH_2-Im, 1-methyl-2-amino-imidazole ring; MWM, Morris water maze; NBM, nucleus basalis of Meynert; PAS, peripheral anionic site; PBS, phosphate-buffered saline; Th-T, thioflavin-T; TLC, thin-layer chromatography.

REFERENCES

(1) Coulthard, E., Singh-Curry, V., and Husain, M. (2006) Treatment of attention deficits in neurological disorders. *Curr. Opin. Neurol. 19*, 613–618.

(2) Klafki, H.-W., Staufenbiel, M., Kornhuber, J., and Wiltfang, J. (2006) Therapeutic approaches to Alzheimer's disease. *Brain 129*, 2840–2855.

(3) Claassen, J. A. H. R., and Jansen, R. W. M. M. (2006) Cholinergically Mediated Augmentation of Cerebral Perfusion in Alzheimer's Disease and Related Cognitive Disorders: The Cholinergic-Vascular Hypothesis. *Journals Gerontol. Ser. A Biol. Sci. Med. Sci. 61*, 267–271.

(4) Li, Q., Yang, H., Chen, Y., and Sun, H. (2017) Recent progress in the identification of selective butyrylcholinesterase inhibitors for Alzheimer's disease. *Eur. J. Med. Chem. 132*, 294–309.

(5) Desai, A. K., and Grossberg, G. T. (2005) Rivastigmine for Alzheimer's disease. *Expert Rev. Neurother. 5*, 563–580.

(6) Vassar, R., Bennett, B. D., Babu-Khan, S., Kahn, S., Mendiaz, E. A., Denis, P., Teplow, D. B., Ross, S., Amarante, P., Loeloff, R., Luo, Y., Fisher, S., Fuller, J., Edenson, S., Lile, J., Jarosinski, M. A., Biere, A. L., Curran, E., Burgess, T., Louis, J. C., Collins, F., Treanor, J., Rogers, G., and Citron, M. (1999) Beta-secretase cleavage of Alzheimer's amyloid precursor protein by the transmembrane aspartic protease BACE. *Science 286*, 735–741.

(7) Viayna, E., Sabate, R., and Muñoz-Torrero, D. (2013) Dual Inhibitors of β-Amyloid Aggregation and Acetylcholinesterase as Multi-Target Anti-Alzheimer Drug Candidates. *Curr. Top. Med. Chem. 13*, 1820–1842.

(8) Costanzo, P., Cariati, L., Desiderio, D., Sgammato, R., Lamberti, A., Arcone, R., Salerno, R., Nardi, M., Masullo, M., and Oliverio, M. (2016) Design, Synthesis, and Evaluation of

Donepezil-Like Compounds as AChE and BACE-1 Inhibitors. *ACS Med. Chem. Lett. 7*, 470–475.

(9) Nguyen, V. T., To, D. C., Tran, M. H., Oh, S. H., Kim, J. A., Ali, M. Y., Woo, M.-H., Choi, J. S., and Min, B. S. (2015) Isolation of cholinesterase and β-secretase 1 inhibiting compounds from Lycopodiella cernua. *Bioorg. Med. Chem. 23*, 3126–3134.

(10) Turk, T., Maček, P., and Šuput, D. (1995) Inhibition of acetylcholinesterase by a pseudozoanthoxanthin-like compound isolated from the zoanthid Parazoanthus axinellae (O. Schmidt). *Toxicon 33*, 133–142.

(11) Stachel, S. J., Coburn, C. A., Rush, D., Jones, K. L. G., Zhu, H., Rajapakse, H., Graham, S. L., Simon, A., Katharine Holloway, M., Allison, T. J., Munshi, S. K., Espeseth, A. S., Zuck, P., Colussi, D., Wolfe, A., Pietrak, B. L., Lai, M.-T., and Vacca, J. P. (2009) Discovery of aminoheterocycles as a novel beta-secretase inhibitor class: pH dependence on binding activity part 1. *Bioorg. Med. Chem. Lett. 19*, 2977–80.

(12) Cavalli, A., Bolognesi, M. L., Capsoni, S., Andrisano, V., Bartolini, M., Margotti, E., Cattaneo, A., Recanatini, M., and Melchiorre, C. (2007) A small molecule targeting the multifactorial nature of Alzheimer's disease. *Angew. Chem. Int. Ed. Engl. 46*, 3689–3692.

(13) Bolognesi, M. L., Banzi, R., Bartolini, M., Cavalli, A., Tarozzi, A., Andrisano, V., Minarini, A., Rosini, M., Tumiatti, V., Bergamini, C., Fato, R., Lenaz, G., Hrelia, P., Cattaneo, A., Recanatini, M., and Melchiorre, C. (2007) Novel class of quinone-bearing polyamines as multi-target-directed ligands to combat Alzheimer's disease. *J. Med. Chem. 50*, 4882–4897.

(14) Bolognesi, M. L., Bartolini, M., Tarozzi, A., Morroni, F., Lizzi, F., Milelli, A., Minarini, A., Rosini, M., Hrelia, P., Andrisano, V., and Melchiorre, C. (2011) Multitargeted drugs discovery: balancing anti-amyloid and anticholinesterase capacity in a single chemical entity. *Bioorg. Med. Chem. Lett. 21*, 2655–8.

(15) Bjørsvik, H.-R., and Sandtorv, A. H. (2014) Synthesis of Imidazole Alkaloids Originated in Marine Sponges, in *Studies in Natural Products Chemistry*, pp 33–57. Elsevier.

(16) Žula, A., Kikelj, D., and Ilaš, J. (2016) Chemistry of 2-Aminoimidazoles. *J. Heterocycl. Chem. 53*, 345–355.

(17) Albizati, K. F., and Faulkner, D. J. (1985) Stevensine, a novel alkaloid of an unidentified marine sponge. *J. Org. Chem. 50*, 4163–4164.

(18) Khurana, R., Coleman, C., Ionescu-Zanetti, C., Carter, S. A., Krishna, V., Grover, R. K., Roy, R., and Singh, S. (2005) Mechanism of thioflavin T binding to amyloid fibrils. *J. Struct. Biol. 151*, 229–238.

(19) Bucciantini, M., Giannoni, E., Chiti, F., Baroni, F., Formigli, L., Zurdo, J., Taddei, N., Ramponi, G., Dobson, C. M., and Stefani, M. (2002) Inherent toxicity of aggregates implies a common mechanism for protein misfolding diseases. *Nature 416*, 507–511.

(20) Galante, D., Ruggeri, F. S., Dietler, G., Pellistri, F., Gatta, E., Corsaro, A., Florio, T., Perico, A., and D'Arrigo, C. (2016) A critical concentration of N-terminal pyroglutamylated amyloid beta drives the misfolding of Ab1-42 into more toxic aggregates. *Int. J. Biochem. Cell Biol. 79*, 261–270.

(21) Galante, D., Corsaro, A., Florio, T., Vella, S., Pagano, A., Sbrana, F., Vassalli, M., Perico, A., and D'Arrigo, C. (2012) Differential toxicity, conformation and morphology of typical initial aggregation states of Aβ1-42 and Aβpy3-42 beta-amyloids. *Int. J. Biochem. Cell Biol. 44*, 2085–2093.

(22) Fändrich, M. (2012) Oligomeric Intermediates in Amyloid Formation: Structure Determination and Mechanisms of Toxicity. *J. Mol. Biol. 421*, 427–440.

(23) Bartolini, M., Naldi, M., Fiori, J., Valle, F., Biscarini, F., Nicolau, D. V., and Andrisano, V. (2011) Kinetic characterization of amyloid-beta 1–42 aggregation with a multimethodological approach. *Anal. Biochem. 414*, 215–225.

(24) Parbhu, A., Lin, H., Thimm, J., and Lal, R. (2002) Imaging real-time aggregation of amyloid beta protein (1–42) by atomic force microscopy. *Peptides 23*, 1265–1270.

(25) Rispoli, V., Rotiroti, D., Carelli, V., Liberatore, F., Scipione, L., Marra, R., Tortorella, S., and Di Rienzo, B. (2004) Electroencephalographic effects induced by choline pivaloyl esters in scopolamine-treated or nucleus basalis magnocellularis lesioned rats. *Pharmacol. Biochem. Behav. 78*, 667–673.

(26) Rispoli, V., Ragusa, S., Nisticò, R., Marra, R., Russo, E., Leo, A., Felicitá, V., and Rotiroti, D. (2013) Huperzine A Restores Cortico-Hippocampal Functional Connectivity after Bilateral AMPA Lesion of the Nucleus Basalis of Meynert. *J. Alzheimers. Dis.*

(27) Rispoli, V., Rotiroti, D., Carelli, V., Liberatore, F., Scipione, L., Marra, R., Giorgioni, G., and Di Stefano, A. (2004) Choline pivaloyl esters improve in rats cognitive and memory performances impaired by scopolamine treatment or lesions of the nucleus basalis of Meynert. *Neurosci. Lett. 356*, 199–202.

(28) Rispoli, V., Marra, R., Costa, N., Scipione, L., Rotiroti, D., De Vita, D., Liberatore, F., and Carelli, V. (2006) Choline pivaloyl ester strengthened the benefit effects of Tacrine and Galantamine on electroencephalographic and cognitive performances in nucleus basalis magnocellularis-lesioned and aged rats. *Pharmacol. Biochem. Behav. 84*, 453–467.

(29) Rispoli, V., Marra, R., Costa, N., Rotiroti, D., Tirassa, P., Scipione, L., De Vita, D., Liberatore, F., and Carelli, V. (2008) Choline pivaloyl ester enhances brain expression of both nerve growth factor and high-affinity receptor TrkA, and reverses memory and cognitive deficits, in rats with excitotoxic lesion of nucleus basalis magnocellularis. *Behav. Brain Res. 190*, 22–32.

(30) Carelli V, Liberatore F, Scipione L, Cardellini M, Rotiroti D, R. V. (2006) Choline

derivatives for the treatment of Alzheimer's disease. Bulletin 2006-10, European Patent.

(31) Cossette, P., Umbriaco, D., Zamar, N., Hamel, E., and Descarries, L. (1993) Recovery of choline acetyltransferase activity without sprouting of the residual acetylcholine innervation in adult rat cerebral cortex after lesion of the nucleus basalis. *Brain Res. 630*, 195–206.

(32) Shaughnessy, L. W., Mundy, W. R., Tilson, H. A., and Barone, S. (1998) Time course of changes in cholinergic and neurotrophin-related markers after infusion of colchicine into the basal forebrain. *Brain Res. 781*, 62–77.

(33) Morris, G. M., Huey, R., Lindstrom, W., Sanner, M. F., Belew, R. K., Goodsell, D. S., and Olson, A. J. (2009) AutoDock4 and AutoDockTools4: Automated docking with selective receptor flexibility. *J. Comput. Chem. 30*, 2785–2791.

(34) Schmidt, M. W., Baldridge, K. K., Boatz, J. A., Elbert, S. T., Gordon, M. S., Jensen, J. H., Koseki, S., Matsunaga, N., Nguyen, K. A., Su, S., Windus, T. L., Dupuis, M., and Montgomery, J. A. (1993) General atomic and molecular electronic structure system. *J. Comput. Chem. 14*, 1347–1363.

(35) Fox, T., and Kollman, P. A. (1998) Application of the RESP Methodology in the Parametrization of Organic Solvents. *J. Phys. Chem. B 102*, 8070–8079.

(36) Eswar, N., Webb, B., Marti-Renom, M. A., Madhusudhan, M. S., Eramian, D., Shen, M.-Y., Pieper, U., and Sali, A. (2006) Comparative Protein Structure Modeling Using Modeller, in *Current Protocols in Bioinformatics*, p 5.6.1-5.6.30. John Wiley & Sons, Inc., Hoboken, NJ, USA.

(37) Case, D. A., Darden, T. A., Cheatham III, T. E., Simmerling, C. L., Wang, J., Duke, R. E., Luo, R., Walker, R. C., Zhang, W., Merz, K. M., Roberts, B., Hayik, S., Roitberg, A., Seabra, G., Swails, J., Goetz, A. W., Kolossváry, I., Wong, K. F., Paesani, F., Vanicek, J., Wolf, R. M., Liu, J., Wu, X., Brozell, S. R., Steinbrecher, T., Gohlke, H., Cai, Q., Ye, X., Hsieh, M. J., Cui, G., Roe, D. R., Mathews, D. H., Seetin, M. G., Salomon-Ferrer, R., Sagui, C., Babin, V., Luchko, T., Gusarov, S., Kovalenko, A., and Kollman, P. A. (2012) AMBER 12, University of California, San Francisco. University of California, San Francisco.

(38) Wang, J., Wolf, R. M., Caldwell, J. W., Kollman, P. A., and Case, D. A. (2004) Development and testing of a general amber force field. *J. Comput. Chem. 25*, 1157–1174.

(39) Ryckaert, J.-P., Ciccotti, G., and Berendsen, H. J. C. (1977) Numerical integration of the cartesian equations of motion of a system with constraints: molecular dynamics of n-alkanes. *J. Comput. Phys. 23*, 327–341.

(40) Baker, N. A., Sept, D., Joseph, S., Holst, M. J., and McCammon, J. A. (2001) Electrostatics of nanosystems: application to microtubules and the ribosome. *Proc. Natl. Acad. Sci. U. S. A. 98*, 10037–41.

(41) Pettersen, E. F., Goddard, T. D., Huang, C. C., Couch, G. S., Greenblatt, D. M., Meng, E.

C., and Ferrin, T. E. (2004) UCSF Chimera--a visualization system for exploratory research and analysis. *J. Comput. Chem. 25*, 1605–1612.

(42) Schwartz, R. E., Yunker, M. B., Scheuer, P. J., and Ottersen, T. (1979) Pseudozoanthoxanthins from gold coral. *Can. J. Chem. 57*, 1707–1711.

(43) de Nanteuil, G., Ahond, A., Guilhem, J., Poupat, C., Dau, E. T. H., Potier, P., Pusset, M., Pusset, J., and Laboute, P. (1985) Invertebres marins du lagon neo-caledonien-V: Isolement et identification des metabolites d'une nouvelle espece de spongiaire, pseudaxinyssa cantharella. *Tetrahedron 41*, 6019–6033.

(44) Ellman, G. L., Courtney, K. D., Andres, V., and Featherstone, R. M. (1961) A new and rapid colorimetric determination of acetylcholinesterase activity. *Biochem. Pharmacol. 7*, 88–95.

(45) Dixon, M. (1953) The determination of enzyme inhibitor constants. *Biochem. J. 55*, 170–171.

(46) Mancini, F., Naldi, M., Cavrini, V., and Andrisano, V. (2007) Multiwell fluorometric and colorimetric microassays for the evaluation of beta-secretase (BACE-1) inhibitors. *Anal. Bioanal. Chem. 388*, 1175–1183.

(47) Camps, P., Formosa, X., Galdeano, C., Muñoz-Torrero, D., Ramírez, L., Gómez, E., Isambert, N., Lavilla, R., Badia, A., Clos, M. V., Bartolini, M., Mancini, F., Andrisano, V., Arce, M. P., Rodríguez-Franco, M. I., Huertas, O., Dafni, T., and Luque, F. J. (2009) Pyrano[3,2- c]quinoline−6-Chlorotacrine Hybrids as a Novel Family of Acetylcholinesterase- and β-Amyloid-Directed Anti-Alzheimer Compounds. *J. Med. Chem. 52*, 5365–5379.

(48) Corsaro, A., Thellung, S., Bucciarelli, T., Scotti, L., Chiovitti, K., Villa, V., D'Arrigo, C., Aceto, A., and Florio, T. (2011) High hydrophobic amino acid exposure is responsible of the neurotoxic effects induced by E200K or D202N disease-related mutations of the human prion protein. *Int. J. Biochem. Cell Biol. 43*, 372–382.

(49) Carrotta, R., Canale, C., Diaspro, A., Trapani, A., Biagio, P. L. S., and Bulone, D. (2012) Inhibiting effect of αs1-casein on Aβ1–40 fibrillogenesis. *Biochim. Biophys. Acta - Gen. Subj. 1820*, 124–132.

(50) Nečas, D., and Klapetek, P. (2012) Gwyddion: an open-source software for SPM data analysis. *Open Phys. 10*, 181–188.

(51) Morris, R. (1984) Developments of a water-maze procedure for studying spatial learning in the rat. *J. Neurosci. Methods 11*, 47–60.

For Table of Contents Use Only

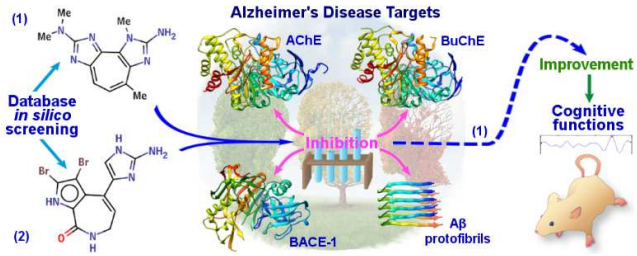

Manuscript: ***In silico identification and experimental validation of novel anti-Alzheimer's multitargeted ligands from marine source.***

Authors: Vitale R.M., Rispoli V., Desiderio D., Sgammato R., Thellung S., Canale C., Vassalli M., Carbone M., Ciavatta M.L., Mollo E., Felicità V., Arcone R., Gavagnin M., Masullo M., Florio T., Amodeo P.